# Newly Discovered Triassic Lithium Deposits in the Dahongliutan Area, NorthWest China: A Case Study for the Detection of Lithium-Bearing Pegmatite Deposits in Rugged Terrains Using Remote-Sensing Data and Images

Yongbao Gao[1]*, Leon Bagas[1,2], Kan Li[1], Moushun Jin[1], Yuegao Liu[3] and Jiaxin Teng[1]

[1]Key Laboratory for the Study of Focused Magmatism and Giant Ore Deposits of Ministry of Natural Resources, Xi'an Center of China Geological Survey, Xi'an, China, [2]Centre for Exploration Targeting (CET), The University of Western Australia, Crawley, WA, Australia, [3]CAS Key Laboratory for Experimental Study Under Deep-sea Extreme Conditions, Institute of Deep-sea Science and Engineering, Chinese Academy of Sciences, Sanya, China

Rare metals, such as lithium and cobalt used in rechargeable batteries, have increased in value as demands for them escalates. Concentrations of lithium-bearing minerals are found in closed-basin brines, granitic pegmatites, and associated granitic rocks containing spodumene $(LiAl(SiO_3)_2)$ and various other economic minerals. The recently discovered Dahongliutan Li mineral occurrences are hosted by a pegmatite dyke swarm in NW China, in an area that is also prospective for Be, Rb, Nb, and Ta mineralisation. However, the high altitude and steep topography in the area make it extremely difficult to explore for mineralisation. A combination of geochemical methods, geological mapping, and high-resolution remotely sensed multispectral imagery has been used in this study to pinpoint potential locations of pegmatite-hosted Li occurrences. The exploration method developed has led to the discovery many large Li mineral occurrences in the Bayankala Fold Belt, including the 505, 507, north 509, and South Fulugou 1# and 2# mineral occurrences (documented here) with a combined resource of over 1.7 million tonnes (Mt). The laser ablation multi-receiver inductively coupled plasma mass spectrometer (LA-MC-ICP-MS) $^{206}Pb/^{207}Pb$-$^{238}U/^{207}Pb$ isochron age of the mineralised pegmatite is 223 ± 11 Ma (N = 44, MSWD = 2.1). The $^{40}Ar/^{39}Ar$ plateau age of muscovite in the mineralised pegmatite dates between 197 ± 1 and 185 ± 1 Ma. These dates show that these granitic pegmatites (with a monzogranitic composition) were emplaced during the Late Triassic coeval with magmatism in the region. Our data show that the Li mineralisation in the Dahongliutan area has a similar age and genesis as the pegmatite-hosted deposits of the Jiajika area in the western Sichuan Province. This indicates that the Dahongliutan area is highly prospective of various pegmatite-hosted mineral deposits.

**Keywords: dahongliutan area, U-Pb and Ar-Ar dating, triassic, Li-bearing pegmatite, satellite remote sensing, resource potential**

# INTRODUCTION

Lithium compounds are widely used in the aerospace, chemical, pharmaceutical, and new energy industries (Li et al., 2007; Li et al., 2014). With continued breakthroughs in the research and development of rechargeable batteries, lithium has become a significant commodity (Wang et al., 2018). Lithium deposits can be divided into the common brine- and less common pegmatite-, granite-, and clay-hosted types (Munk et al., 2018; Wang et al., 2019). Of these, the brine types are the largest in size, but the pegmatite-hosted deposits can be more valuable and easier to mine, especially if they include combinations of high-grade Be, Nb, Ta, Rb or Cs deposits (Linnen et al., 2012; Li et al., 2014; Munk et al., 2018; Goodenough et al., 2019; Wang et al., 2019). The Li-bearing minerals in pegmatites include silicates, spodumene, mica accumulates in pegmatite veins, and in the late stages of magmatic crystallisation accompanied by volatile-rich hydrothermal fluids (London, 2018). Many of these deposits have been discovered with geological mapping, geochemical sampling and interpretation of remote sensing (satellite) images in terrains that are not mountainous.

The method of using satellite images for mineral exploration begins with the compilation of information, which is commonly done in a Geographic Information System (GIS) environment. This includes available records of exploration, geo-referenced geological maps, and initial interpretations of satellite images and orthorectified aerial photographs (where available) (Dimmell et al., 2005; Selway et al., 2005; Scogings et al., 2016; Steiner, 2018; Cardoso-Fernandes et al., 2019a; Cardoso-Fernandes et al., 2019b; Steiner, 2019a; Steiner, 2019b; Cardoso-Fernandes et al., 2020a; Cardoso-Fernandes et al., 2020b). This data is initially used to define areas that might be prospective for economic concentrations of minerals, where regional geochemistry sampling and initial geological mapping is commenced. However, these methods are not always viable in mountainous terranes such as in the Tibetan Plateau at elevations around 4,000 km above sea level. In a favourable environment, the geochemical sampling involves rock, stream-sediment, and soil sampling, which are generally considered important tool for defining vectors towards LCT pegmatites (c.f. Steiner, 2019b), but this is not easily achieved in steep mountainous terrains such as the Tibetan Plateau, and other, safer, techniques must be applied.

Remote sensing data obtained from Advanced Spaceborne Thermal Emission and Reflection Radiometer (ASTER), Sentinel-2, Landsat-5 and Landsat-8 satellites, are commonly used to detect Li-bearing pegmatites (Mendes et al., 2017; Cardoso-Fernandes et al., 2018, Cardoso-Fernandes et al., 2019a). These methods aimed to detect hydrothermally altered zones associated with mineralisation and Li-bearing minerals directly (Cardoso-Fernandes et al., 2019a). The results were often indecisive because of the limitations of the band ratios used, except for the ASTER sensor that can detect clays associated with alteration zones, and vegetation often masked the location of mineralised zones (Cardoso-Fernandes et al., 2019b). Remote sensing technology has been refined significantly in recent years with the rapid development of new, high-resolution sensors in, for example, IKONOS; DigitalGlobeQuickBird; SPOT-5; Worldview-2;

Worldview-3; Gaofen-1; Gaofen-2; and Gaofen-7 satellites (Table 1). The application of remote sensing technology is becoming increasingly widespread in distinguishing the nature of the geology and mineral exploration in remote regions. This includes the recognition of alteration assemblages associated with mineral deposits in remote sensing data at a high-resolution allowing the recognition of pegmatites at a metre-scale, whereas the tradition methods dealt with resolutions at a 10-m scale (Moradi et al., 2014; Pour and Hashim, 2015).

Northwestern China is beginning to be recognised as a highly prospective part of China for various mineral commodities, including sedimentary and metamorphic Fe, porphyry Cu-Mo, skarn polymetallic deposits, and lithium deposits (Yang et al., 2003; Chen et al., 2009; Yao et al., 2009). The two known types of lithium deposit are: 1) those associated with granites and pegmatites; and 2) those in arid environments found in brine lakes and salt pans containing soluble carbonate and chloride salts of lithium (e.g. deposits in Chile). The most common lithium deposits hosted by granite and pegmatite contain spodumene ($LiAl(SiO_3)_2$), such as at the Greenbushes mine in Western Australia. Previous studies targeted spodumene with remote sensing involving spectroscopic tests on ore-forming minerals related to pegmatite in the Jiajika region of western Sichuan Province (Dai et al., 2017; Dai et al., 2018). The application of remote sensing has not been applied on pegmatite dykes and veins in the Dahongliutan area of the Bayankala Fold Belt until now (Figure 1A).

This contribution documents a new method for identifying prospective regions containing spodumene-bearing granitic pegmatite veins. This involves processing high-resolution remote-sensing and multispectral remote sensing images including Worldview-2, Worldview-3 and ASTER images, and regional geochemical and geological data in the mountainous Dahongliutan area (Figure 1). The technique has led to the discovery of many large Li occurrences with a resource of over 1.7 Mt, which includes the 505, 507, north 509, and South Fulugou 1# and 2# mineral occurrences (Figure 1). The method is a breakthrough in allowing for a rapid and efficient exploration for pegmatite-type mineral deposits in deeply incised terrains with high-altitudes, which can be of great interest to exploration and mining companies. This paper introduces our new exploration method, evaluates its effectiveness, introduces the geological characteristics of newly discovered Li deposits, and explores the potential of regional resources in the West Kunlun and Karakoram regions. Furthermore, knowing the timing of these pegmatites and their spatially associated granitic hosts are also important, because this allows us to better constrain the tectonic setting involved, and answer the following questions. Have these intrusions been emplaced in a subduction, collisional or post-collisional setting, and how does this relate to the Li prospectivity in other regions in China?

# GEOLOGICAL SETTING

The recently discovered Dahongliutan mineralised zone is in the Bayankala Fold Belt, which comprises the West Kunlun Orogen

| No | Satellite name | Spectral range (nm) | Number of bands | Spatial resolution (m) |
|----|----------------|---------------------|-----------------|------------------------|
| 1 | Landsat5 | 450–2,350 | 7 | 30 |
| 2 | Landsat7 | 450–2,350 | 7 | 15 |
| 3 | Landsat8 | 450–2,350 | 8 | 15 |
| 4 | Sentinel-2 | 443–2,190 | 13 | 10–60 |
| 5 | ASTER | 520–2,430 | 14 | 15 |
| 6 | SPOT-5 | 490–1780 | 4 | 2.5 |
| 7 | GF-1 | 450–890 | 4 | 2 |
| 8 | IKONOS | 450–850 | 4 | 1 |
| 9 | QUICKBIRD | 450–900 | 4 | 0.6 |
| 10 | GF-2 | 450–890 | 4 | 1 |
| 11 | Worldview-2 | 400–1,040 | 8 | 0.5 |
| 12 | Worldview-3 | 400–2,365 | 16 | 0.3 |

and Tashkurgan-Tianshuihai terranes in the southern part of the Xinjiang Province (**Figure 1A**). The combined area borders the Tibetan Plateau to the south and Tarim Block to the north (**Figure 1A**). The region includes Precambrian to Cenozoic units recording a complex geological evolution, such as subduction of oceanic plates, and collisional tectonics involving the West Kunlun and Tashkurgan-Tianshui terranes and Tarim Block during the early Paleozoic and Mesozoic (Mattern and Schneider, 2000; Xiao et al., 2003; Jiang et al., 2013; Wang et al., 2017; Yan et al., 2018).

There is a wide variety of mineral deposits in the region, including: 1) sedimentary Mn and volcanogenic massive sulfide deposits in the West Kunlun Orogen (Jia et al., 1999; Gao et al., 2017; Gao et al., 2018); 2) sedimentary Fe in banded iron-formation and giant Zn-Pb non-sulfide deposits in the Tashkurgan-Tianshui terranes (Chen et al., 2019; Gao et al., 2019; Zhang et al., 2019; Gao et al., 2020); and 3) pegmatite-hosted Li(-Be) deposits in the Bayankala Fold Belt (Li et al., 2019). This multi-element mineralised zone in the study area extends for over 50 km with a width of over 5 km and is structurally controlled by the Dahongliutan-Guozhacuo and Kangxiwa faults (**Figure 1B**).

The exposed rocks in the study area are assigned to the Paleoproterozoic Kangxiwa Complex, Permian Huangyangling Group, and Triassic Bayankala Formation (Qiao et al., 2015; Teng and Gao, 2019). The Kangxiwa Complex includes a sequence of biotite schist, biotite-plagioclase gneiss, and marble metamorphosed up to granulite facies. The Huangyangling Group consists of fine-grained clastic and minor carbonate and intermediate to mafic volcanic rocks. The Bayankala Formation is a deep-water turbiditic succession of clastic units and minor carbonate rocks, which host spodumene-bearing pegmatite veins and dykes. The formation is subdivided into: 1) an early member consisting of lithic sandstone, gravel beds and shale; 2) a central member consisting of quartz (-feldspar) sandstone, shale, and marlstone; and 3) a late member consisting of feldspathic quartz sandstone, and siltstone.

Major faults in the region trend SE including the Kangxiwa, Dahongliutan-Guozhacuo, and Qitaidaban faults (**Figure 1B**). The steep (65°–85°) NE-dipping and long-lived Kangxiwa Fault forms the boundary between the Bayankala Fold Belt to the south and South Kunlun Terrane to the north (Liu et al., 2003). Xu et al.
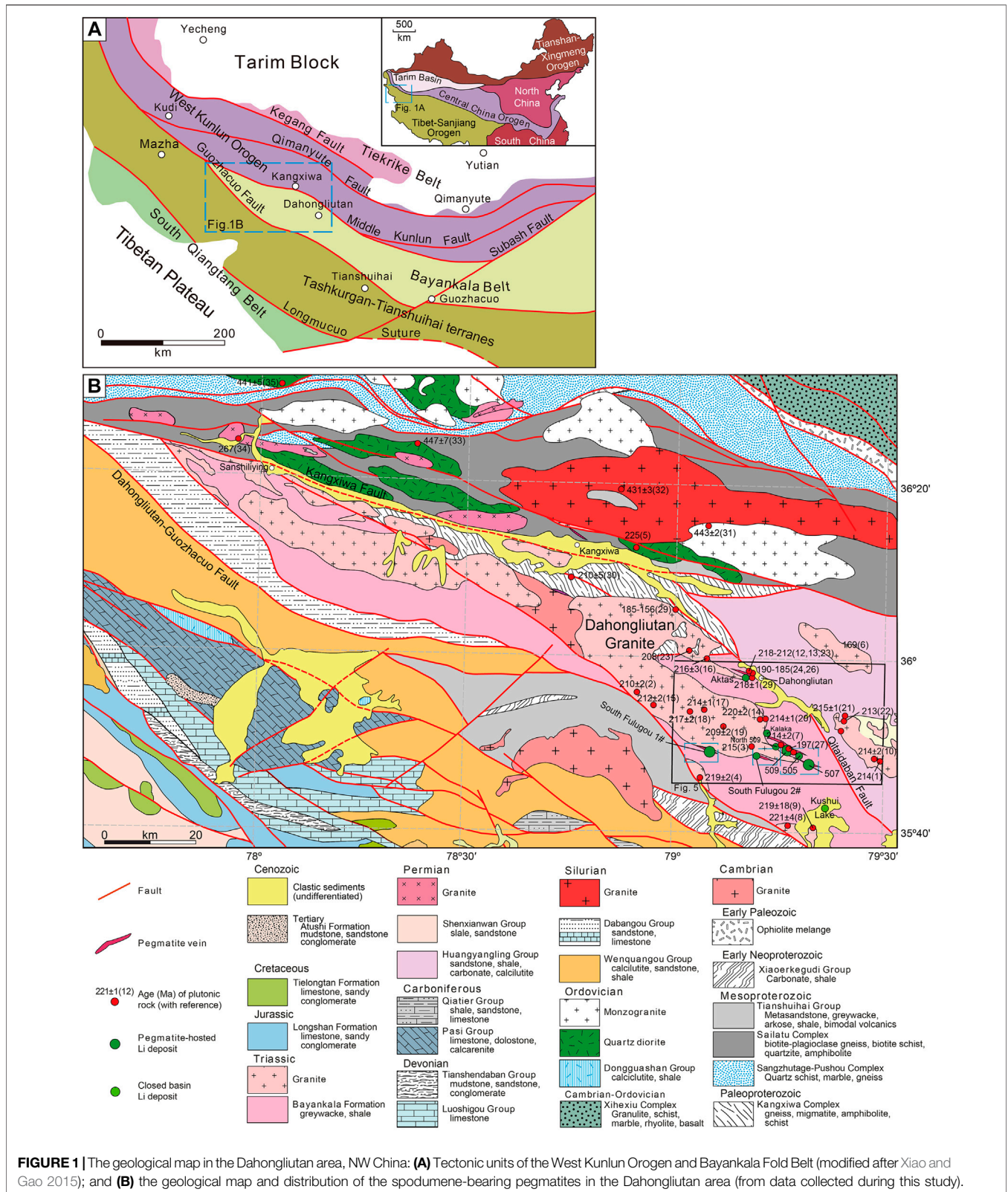
(2007) and He et al. (2009) note that dextral ductile strike-slip movement along the fault developed between ca. 445–428 Ma, and sinistral strike-slip movement developed during ca. 250, 203, 102–125 and 10 Ma. The fault has controlled the deposition of sedimentary successions and the emplacement of magmatic rocks during the Paleozoic to Mesozoic.

The SE-trending Dahongliutan-Guozhacuo Fault forms the boundary between the Bayankala Fold Belt and Tashkurgan-Tianshuihai terranes (**Figure 1A**). Chen et al. (2010) observe that the fault dips between 50° and 75° NE, was active as a ductile strike-slip fault during ca. 150, 122, and 106 Ma, and might be the western extension of the Altyn-Tagh Fault. Reactivation of the fault included SE-trending thrusting and eastward trending sinistral strike-slip movement depending on the orientation of the fault zone (**Figure 1B**).

The SSE-trending Qitaidaban Fault forms the boundary between the Huangyangling Group and Bayankala Formation. The foliation in the fault zone dips 40°–60° SW and NE, and has been active as an early ductile strike-slip fault and reactivated as a brittle strike-slip fault. Mesozoic and SE-trending intermediate to felsic intrusive rocks are widespread subparallel to the Kangxiwa Fault. This includes Cambrian monzogranite, ca. 223–209 Ma fine-to medium-grained biotite monzogranite, diorite, granodiorite, biotite-quartz diorite, and muscovitic diorite containing garnet and tourmaline (**Supplementary Table S1**; Qiao et al., 2015; Wei et al., 2017).

The Li deposits and occurrences in the Dahongliutan area are hosted by pegmatite dykes along the margin of the Triassic Dahongliutan Granite (**Figure 1**). The dykes form a series of clusters or swarms up to 50-km-long at the Aktas, Kalaka, 509, 505, 507, north 509, and South Fulugou 1# and 2# Li deposits (**Figure 1B**). Of these, the medium-size Aktas Li–Be–Ta–Nb pegmatite-hosted deposit is in schist on the northeastern side of the Dahongliutan Granite and has been studied in detail (Yan et al., 2018). The Aktas deposit includes 10 pegmatites containing Li-Be-Nb-Ta mineralisation in the "90" and "91" vein clusters have been evaluated. Detailed diamond drilling has been used to estimate a resource of 0.085 Mt averaging 1.5% $Li_2O$, 0.04% BeO, 0.09% $Rb_2O$, and 0.024% $(Nb + Ta)_2O_5$ (Teng and Gao, 2019).

The Aktas deposit yields LA–ICP–MS U–Pb columbite-(Fe) and cassiterite ages of ca. 215 Ma (Yan et al., 2018). Many

FIGURE 1 | The geological map in the Dahongliutan area, NW China: (A) Tectonic units of the West Kunlun Orogen and Bayankala Fold Belt (modified after Xiao and Gao 2015); and (B) the geological map and distribution of the spodumene-bearing pegmatites in the Dahongliutan area (from data collected during this study).

pegmatite veins and dykes around the deposit are anomalous in Li–Be–Ta–Nb, but only 10 have been found to economic with lengths between 180 and 300 m long and up to 40 m wide. The

dykes and veins trend southeast and dip steeply (60–80°) SW around the Dahongliutan Granite forming zones with barren muscovite-microcline-type pegmatites in the central zone

followed outward by Be-mineralised muscovite-microcline-albite-type pegmatites to a Li–Ta–Nb-mineralised zone containing quartz-albite-spodumene-type pegmatites (Zhou et al., 2011; Yan et al., 2018; Teng and Gao 2019; Cao et al., 2020).

The 509 deposit includes 13 pegmatite-hosted orebodies with a combined resource of 0.24 Mt averaging 1.75% $Li_2O$, 0.14% BeO and 0.12% $Rb_2O$ hosted by pegmatite veins in the Bayankala Formation and along the edge of the Dahongliutan Granite (Peng et al., 2018). The Sixth Geological Brigade of the Xinjiang Geological and Mineral Bureau evaluated the Kalaka Li deposit with a ~0.1 Mt resource averaging 0.92% $Li_2O$, 0.06% BeO and 0.10% $Rb_2O$ hosted by 18 pegmatites. To date, the Dahongliutan pegmatite field has an estimated resource of over 2 Mt averaging 1.5% $Li_2O$ in a swarm of pegmatite dykes extending over 50 km in a northward to northwest direction (Teng and Gao, 2019).
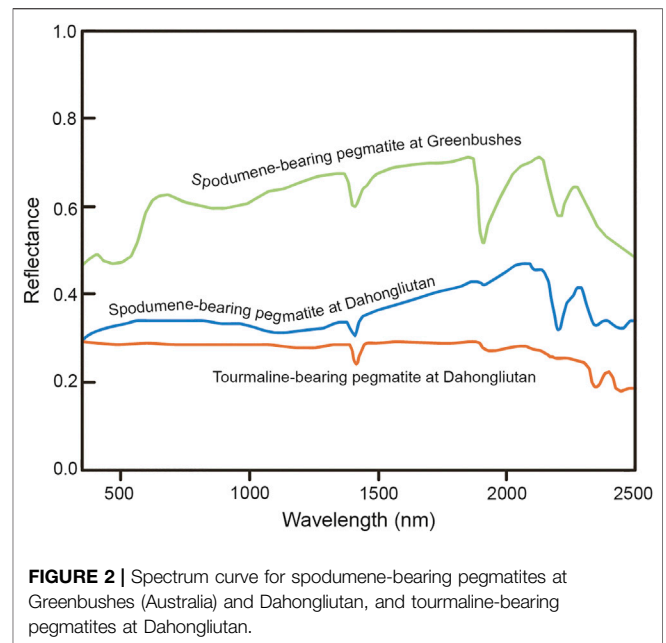
## METHODS USED FOR DISCOVERING THE LITHIUM MINERALISATION

### Geological and Spectral Basis

Reflectance spectra were acquired from samples on the ground surface using an Analytical Spectral Device (ASD) FieldSpec spectrometer with a spectral range of 350–2,500 nm and a nominal resolution of 1 nm. Spodumene-bearing pegmatites were collected from Greenbushes in Western Australia, and spodumene-bearing pegmatites and tourmaline-mica pegmatites from the Dahongliutan area in the Kunlun region of NW China for spectroscopic testing and comparison. The country rocks in both areas are sedimentary rocks, which were not sampled.

All samples were photographed for reference prior to analyses and the illumination of samples provided by a halogen lamp positioned at an incidence angle of approximately 10°. The radiance spectrum from the sample was collected with the ASD pointing at a normal viewing angle to the sample surface and sensing a sample footprint of approximately 30 mm in diameter at a 20 mm standoff distance. The sample radiance spectrum was normalised to that of a standard 99% white reference panel collected before measurement of each sample (Liu et al., 2017a; Liu et al., 2017b). The surface reflectance measurements were taken at 20 spots over each plot, and for each measurement, the ASD spectrometer was kept stationary and ~100 consecutively acquired spectra were recorded to reduce the noise level. The reflectance spectra for minerals are typically unique, and some minerals have distinct bands of absorption and reflection corresponding to remote-sensing image bands. The correlation between the image bands and minerals can be enhanced and extracted by mathematical operations to provide relevant information for exploration (e.g. Kendall, 1975; Hunt and Ashley, 1979; Gan et al., 2003).

We found that the spodumene crystals hosted by pegmatites in the Dahongliutan study area are: 1) columnar, granular, or forms plates; 2) vary from hoary, grey-green, emerald, purple, or yellow in colour; 3) have a hardness of 6.5–7; and 4) have a density of



**FIGURE 2 |** Spectrum curve for spodumene-bearing pegmatites at Greenbushes (Australia) and Dahongliutan, and tourmaline-bearing pegmatites at Dahongliutan.

3.03–3.22 $g/cm^3$. We also found that the spodumene-bearing pegmatite veins typically exhibit a strong first-order absorption value of ~2,200 nm, a second-order absorption value of 2,350 nm, and reflective characteristics between 560 and 760 nm (**Figure 2**). Tourmaline-mica pegmatite dykes in the area do not contain spodumene and locally contain beryl. The dykes are characterised by a strong first-order absorption value of ~2,350 nm without an obvious second-order absorption signature.

Spodumene in the Jiajika area of northern Sichuan Province has the same characteristics, but the spodumene-bearing pegmatites cannot be directly distinguished from barren ones, and the granites (*sensu lato*) in the area have a first-order absorption signature of 1,413 and second-order absorption signature of 2,197 nm (Dai et al., 2017). Country rocks such as sandstone and shale do not have absorption signatures at 2,200 and 2,350 nm.

### The Remote Sensing Interpretation Method

Low-resolution remote sensing satellites include Landsat5, Landsat7 and ASTER, which are characterised by high spectral-resolution. The spectral range includes visible light, near-infrared, and short-wave infrared, with low spatial resolution (15–30 m). Medium-resolution remote sensing satellites include SPOT-5 and Gaofen-1, which are characterised by a resolution of 2–2.5 m and four bands. The spectral range includes visible light, near-infrared, and does not include short-wave infrared. High-resolution remote sensing satellites include IKONOS, QUICKBIRD, GF-2, Worldview-2 and Worldview-3, with a resolution better than 1 m. The IKONOS, QUICKBIRD, and GF-2 have four bands, Worldview-2 has eight bands, and Worldview-3 has 16 bands. The spectrum of Worldview-3 includes visible light, near-infrared, and short-wave infrared. Other high-resolution remote sensing satellites only include visible light and near-

infrared, excluding short-wave infrared. The basic information of various satellites is shown in **Table 1**.

As mentioned above, the spectral ranges of Landsat5, Landsat7, ASTER, and Worldview-3 remote sensing satellites include visible light, near-infrared, and short-wave infrared, which is suitable for the detection of mineral anomalies using remote-sensing data. The spatial resolution of Worldview-3 is two orders of magnitude higher than that of several other remote sensing satellites. Therefore, ASTER and Worldview-3 remote sensing images are better for locating mineral anomalies. The combination of the Worldview-2 and other high-resolution imagery are used to highlight the distribution of pegmatite dykes, and the Worldview-3 data allows us to better identify the location of pegmatite dykes than other satellite data. The handicap, however, is the limited data available for the whole of our study area. It is for this reason we used the combined Worldview-2 and ASTER remote sensing images to pinpointing areas prospective for pegmatite veins.

The WorldView-2 multispectral data acquired during November 3, 2016 were used in this study. According to its manufacturer of the WorldView-2 multispectral sensor, there are the six spectral bands ranging from blue to the near infrared parts of the electromagnetic spectrum, including the Coastal Blue (400–450 nm; B1), Blue (400–510 nm; B2), Green (510–580 nm; B3), Yellow (585–625 nm; B4), Red (630–69 nm; B5), Red-Edge (705–745 nm; B6), Near infrared (770–895; B7) and NearIR-2 (860–1,040 nm; B8) bands, with 0.5 m spatial resolution making it possible to reflect information more clearly from pegmatites. The ASTER multispectral data was acquired during May 2, 2003. The spectral bands detected by modern ASTER remote sensors are now subdivided into the near-infrared and short-spectrum infrared bands giving 14 bands with a resolution of 15 m. ASTER measures reflected radiation in three bands between 520 and 860 nm (i.e. in the visible and near-infrared region, and the VNIR B1-B3) and in six bands from 1,600 to 2,430 nm (i.e. the short-wave infrared region, and SWIR B4-B9). In addition, the emitted radiation is measured at a 90 m spatial resolution in five bands in the 8,120–11,650 nm wavelength region (i.e. the thermal infrared region, and TIR B10-B11) (Bedini, 2011). ASTER images have a high spectral resolution, with six bands in the short-wave infrared spectrum, and it is easy to obtain information from mineralised areas (Jin et al., 2015; Mendes et al., 2017).

The absorption characteristics of spodumene-bearing pegmatites could correspond to each band of remote sensing in Worldview-2 and ASTER images. Spodumene-bearing pegmatites display a reflection feature in the Band 4 (B4) of the Worldview-2 data. In the ASTER bands, the Li-bearing pegmatites are characterised by reflection in B2, strong absorption in B5, and secondary absorption in B8. Using these criteria, the Worldview-2 remote sensing images were enhanced, making it easier to identify the presence of pegmatite clusters through different band combinations and principal component transformations, and the remote sensing anomalies related to the ASTER remote sensing images are extracted to identify the ore-bearing pegmatite veins.

The prospective areas are then ground-proofed with field work and geochemical sampling. The process, which is summarised in **Figure 3**, allows us to quickly focus the exploration activities. This involves a mineral system approach using detailed satellite images to identify pegmatite clusters potentially containing the mineral assemblage spodumene-muscovite-albite-quartz, however this does not guarantee that all the pegmatite clusters host economic concentrations of spodumene. Nonetheless, the method allows us to focus on prospective areas.

## The Recognition of Pegmatite Dykes and Veins in High-Resolution Images

The PCI, ENVI and ERDAS software are used to image remote data from satellites such as Worldview-2 (Zhao, 2003). The PCI software is used for orthographic correction of the WorldView-2 remote sensing images to eliminate geometric position distortions in the remote sensing images caused by surface elevation differences. The ERDAS software is used for multi-spectral and panchromatic band fusion of the WorldView-2 remote sensing images and Mosaic of multi-landscape WorldView-2 remote sensing images. The ENVI software has strong transformation operation functions, which are used to extract remote sensing anomalies from ASTER remote sensing images.

Ortho-rectified images were developed using data from Worldview-2 sensor using bands 5, 3, and 2 (also see *Geological and Spectral Basis*). The Worldview-2 remote sensing image B5 is in the R band, B3 is in the G band, and B2 is in the B band (as part of the red-green-blue spectrum). The combination of the WorldView-2 remote sensing image 532 band is used for enhancement processing. This makes the information content rich and the combined image forms a natural true colour image, which is conducive to visual identification of pegmatites.

Decorrelation analysis was performed using the images with the B5, B3, and B2 combinations to highlight the location of areas prospective for pegmatites. This type of analysis is a process of contrast stretching of the main components of the image. This method can effectively reduce the correlation between different bands and increase the contrast between different geological units (Zhang et al., 2011; Jin et al., 2014). The procedure involves: 1) a principal component forward transformation; 2) a linear enhancement; and 3) a principal component inverse transformation.

The principal component forward transformation statistical analyses combined B5, B3, and B2 images from Worldview-2, then performs the principal component transformation. The linear enhancement involves linear stretching of each principal component obtained by the principal component transformation using the grey value of 0–255 to improve the contrast between distinctive features. The principal component inverse transformation enhances the principal component transform images. Since each principal component has been linearly stretched, it is restored to a band 5-3-2 composite image after the principal component inverse transformation is completed. An informative image is formed when the correlation between the three bands is small. The processed image using these transformations highlights the location of pegmatite dykes as

**FIGURE 3 |** Model showing the steps involved in interpreting remote sensing data.
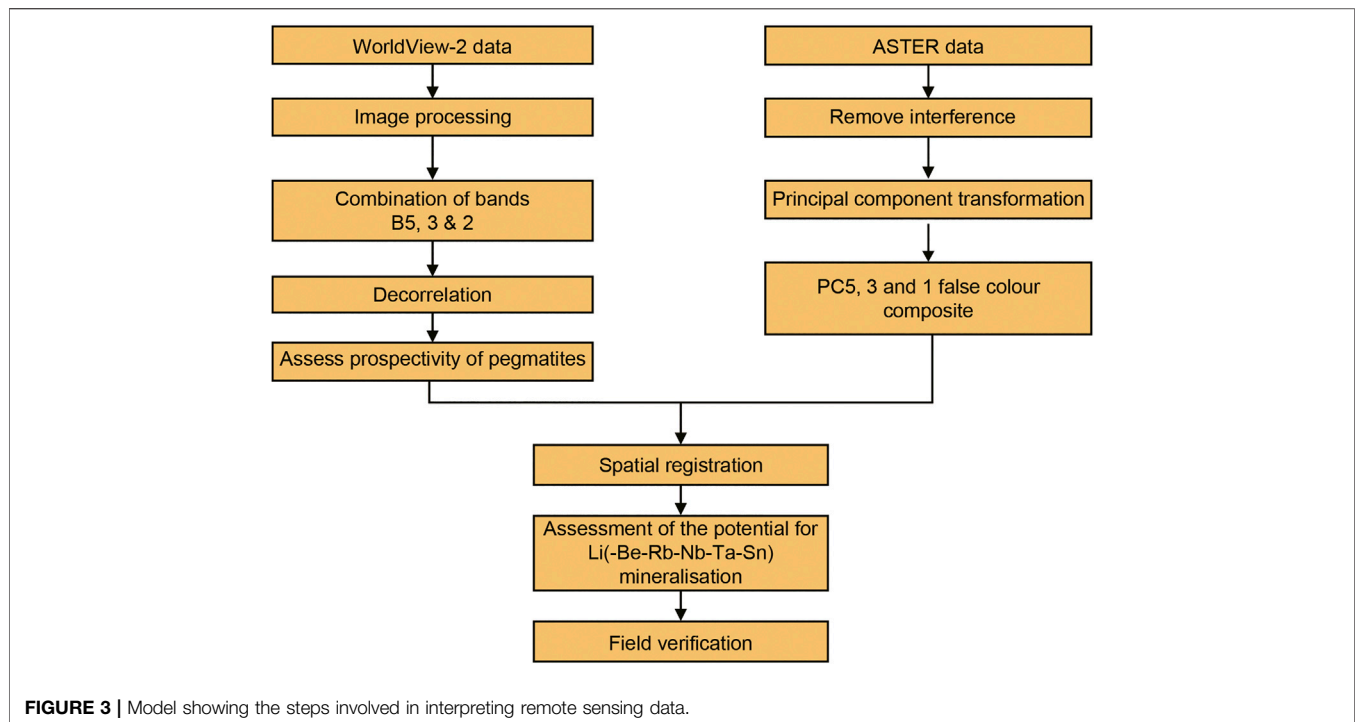
white areas with the country rocks represented by red and fawn coloured areas (**Figures 4,5A**). These prospective pegmatites are small and can only be recognised using detailed images, as discussed in *The Rapid Exploration Method Using Remote Sensing Data*.

## Lithology and Structural Interpretation

The images formed with the combined ASTER B7, B4, and B1 data were used to interpret the lithology and structures hosting pegmatite-type rare metal deposits. The sedimentary rocks are characterised by banding representing bedding, which is discordant at faults or are truncated by granites. The ore-bearing Bayankala Formation is a weakly metamorphosed (up to lower greenschist facies) flysch succession that includes sandstone and shale. The formation is banded in variations of grey on the remote sensing images (**Figures 4**, **5B**).

Intrusive rocks are planar, annular, elliptical, lenticular, have an irregular spatial form, have different geomorphologic combinations, and are discordant with the country rocks. The Dahongliutan Granite intrudes the Bayankala Formation, forms high mountains circumscribed by creeks and rivers, and has a pinkish-red colour on the remote sensing images (**Figure 5B**).

The location of faults is indicated by discordant boundaries between units, and the faults are in or near axial planes of antiformal folds. The structures include normal, reverse, translational and mixed types of faults, and trend northwestern in the Dahongliutan area where they transect areas with subdued topography with a rectangular bend along a river (**Figure 5B**). These structures host the NW-trending pegmatites that form pegmatite-rich clusters (**Figure 5B**).

## Delineation of Pegmatites on Remote-Sensing Images

Features masking the characteristics of prospective geochemical anomalies and geological features on the images include dry rivers, alluvial fans, ice, snow, clouds, lakes, wetlands around snowfields, and swamps. If these features are not accommodated for during the image processing, the signatures for alteration zones are obscured. The purpose of interference removal is to observe different spectral characteristics and more easily choose different mathematical functions, such as ratio analysis and high- and low-end thresholding. The non-target areas and non-target ground objects are included in "interference windows" through digital processing aiming to highlight prospective area. The routine helps develop a basic image for the principal component analysis minimising the influence of interference from non-mineralised rocks and highlighting areas that are anomalous.

Principal component analysis of specific bands can remove the correlation between bands, reduce the data dimension, and concentrate it as much useful information as possible into a small number of image bands. Each principal component often represents unique geological features that do not overlap with each other (Zhang and Yao, 2009).

ASTER bands 1–9 are used in this study for principal component transformations to obtain the nine principal components PC1–9. The principal components PC1 and PC3 in the processed image contain a wealth of information and less noise, and B5 in PC5 participate to a larger extent. Thus, PC5, PC3, and PC1 were used to perform pseudo-colour synthesis producing RGB colour images. Multi-band monochromatic images were synthesised into false colour images highlighting the potential target areas for mineralised pegmatite dykes and veins (**Figures 4**, **5**).
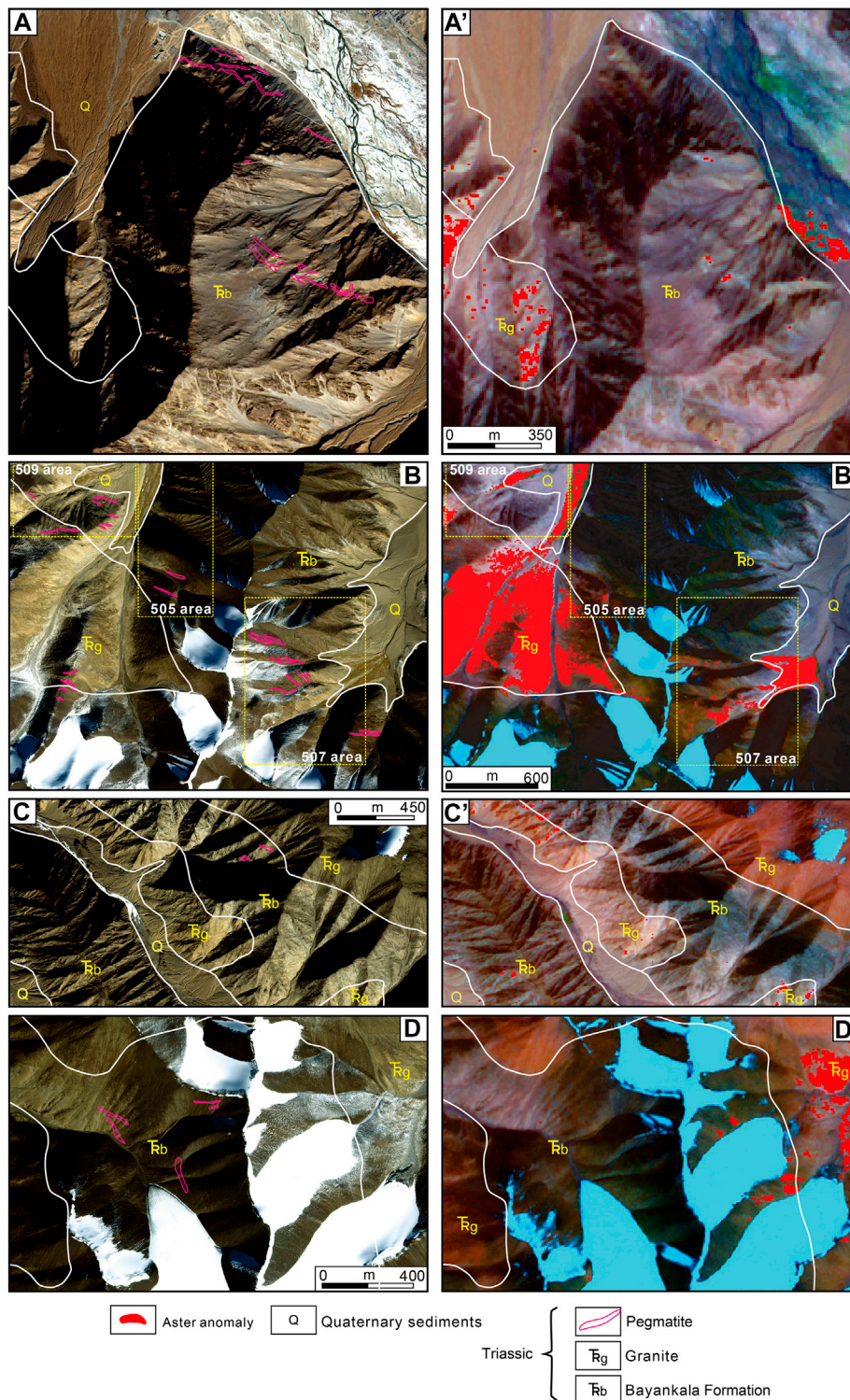
**FIGURE 4 |** Remote sensing images of the Aktas, 505, 507, and South Fulugou 1# and 2# Li deposits: **(A, A′)** Worldview-2 image and Aster image of the Aktas Li deposit; **(B, B′)** Worldview-2 image and Aster image of the 505 and 507 Li deposits; **(C, C′)** Worldview-2 image and Aster image of the South Fulugou 1# Li deposit; **(D, D′)** Worldview-2 image and Aster image of the South Fulugou 2# Li deposit.
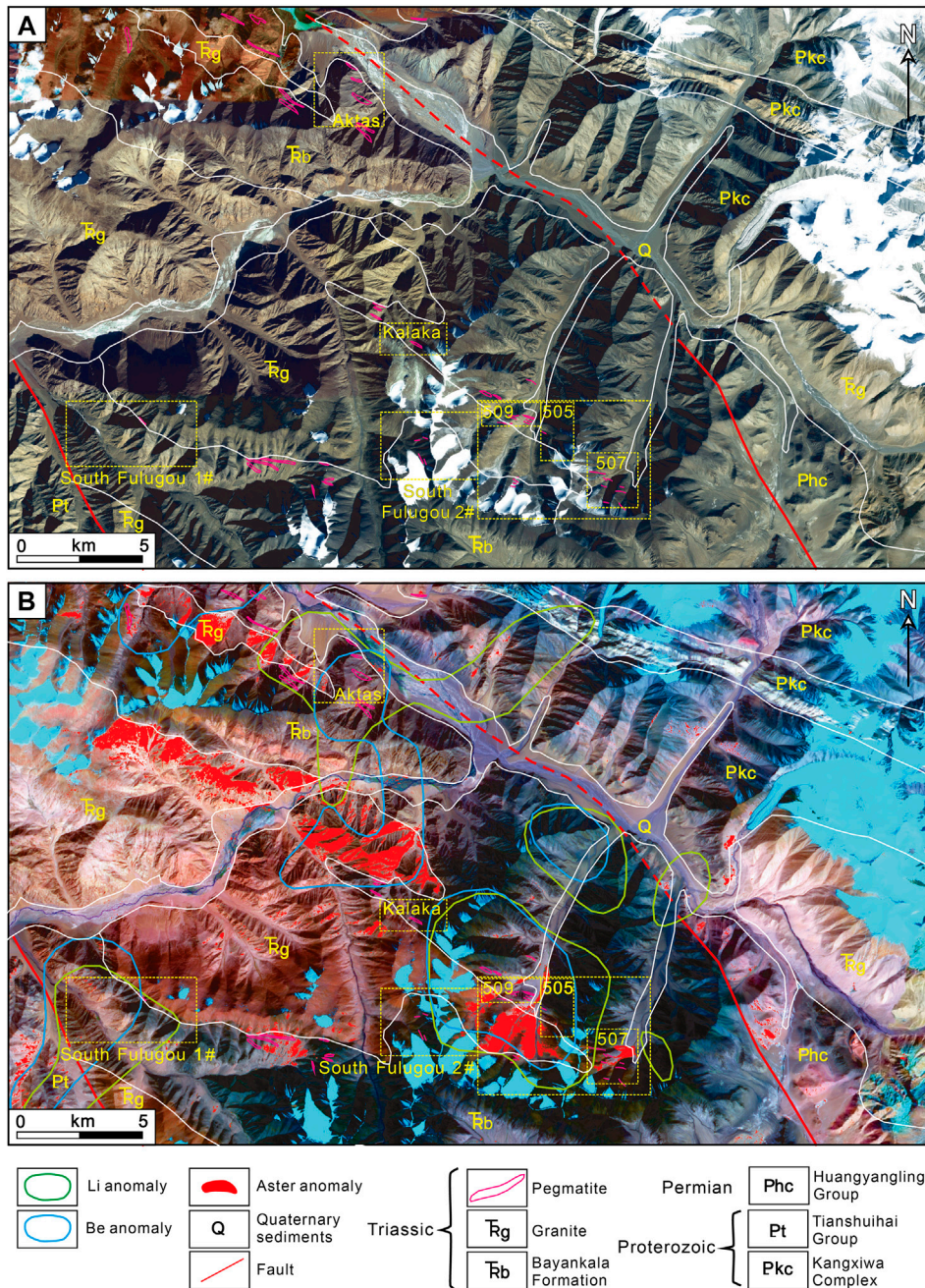
FIGURE 5 | Remote sensing images and prospective sites of Li mineralisation in the Dahongliutan area: (A) Worldview-2 image; and (B) Aster image, and geochemical anomalies of Li and Be.

The Worldview-2 and ASTER images are spatially registered, so that the interpreted location of pegmatite veins spatially overlap on the Worldview-2 image and the rare metal minerals highlighted on the ASTER image. The overlap areas including the 505, 507, and South Fulugou 1# and 2# deposits are designated as highly potential ore-bearing pegmatite locations comprising parts of two or more zones prospective for mineralisation (**Figure 5**).

Based on the comprehensive analysis of available geological information, the ore-forming process and structural controls are compiled. The location of potential ore-bearing pegmatites are then delineated using the combined remote sensing, geological mapping and sampling, which are combined delineating prospective target areas, such as the 505, 507, and South Fulugou 1# and 2# areas (**Figures 4**, **5**).

The areas delineated as being prospective for ore-bearing pegmatites are field checked to determine the reliability and accuracy of the modelled data (**Figure 3**). ASTER remote sensing images were used to extract remote sensing anomalies related to the pegmatite-type rare metal deposits in the study area. These areas were verified in the field (**Figure 5**).

## Sample Collection and Geochemical Analyses

Over 156 geochemical samples weighing a minimum of 1 kg were collected from trenches and diamond-drillhole core in the area considered prospective using satellite images. The samples from the trenches measured around 1 m long, 50 mm deep and 100 mm wide and those from 800 m long half diamond-drillhole core measuring 1 m long and ~70 mm in diameter were collected every 1 m. This ensured complete sampling across pegmatites logged in the core and trenches. The samples were crushed in a steel crusher, "splitted," and then grounded to a 200 mesh ($<74 \mu m$). Sample splitting is the necessary step during the crushing, which ensures the analyses are representative of the rocks sampled.

The rock powder (~100 mg) was dissolved in a Teflon bomb using a mixture of 1 ml $HNO_3$ and 2 ml HF. The Teflon bomb was dried on a hotplate, and then dissolved in 1 ml $HNO_3$. The Teflon bomb was put in a stainless-steel pressure jacket and heated to 180°C in an oven for 36 h. After cooling, the Teflon bomb was opened and placed on a hotplate and evaporated to dryness. The dried sample was refluxed with 1.5 ml of $HNO_3$ and evaporated to dryness again. A further 4 ml of $HNO_3$ was added to the sample and the close bomb was placed in an oven heated to 150°C for 12 h. After cooling, the final solution was diluted to ~50 ml in a polyethylene bottle and prepared for analyses. The analyses of these standards have analytical errors of ±2% for Li, ±2.5% for Rb, and ±5% for low concentrations of Be, Cs, Nb, and Ta. The element compositions were determined using an iCAP RQ ICP-MS at the MNR Key Laboratory for the Study of Focused Magmatism and Giant Ore Deposits, Xi'an Center of China Geological Survey.

## Dating of Mineralisation

Cassiterite coexisting with spodumene was extracted from the centre of the No. 18 orebody (sample 505–2) at the 505 Li deposit for U-Pb isotope dating. The cassiterite measuring 80–150 μm across was selected under a binocular microscope, is reddish brown in colour under transmitted light, and cracks were observed under the reflected light. Cassiterite samples without cracks and inclusions were selected for U-Pb dating using a laser ablation multi-receiver inductively coupled plasma mass spectrometer (LA-MC-ICP-MS) at the Isotope Laboratory of the Tianjin Center of China Geological Survey. The multi-collector inductively coupled plasma mass spectrometer is a Neptune manufactured by Thermo Fisher Company, and the laser is a UP193-FX ArF Excimer Laser produced by the ESI Company in the USA. Li et al. (2009), Hao et al. (2016),

and Cui et al. (2017) describe the operating conditions of the laser ablation system, the ICP-MS instrument, and the data reduction process.

A 193 nm FX laser was used to ablate the cassiterites with a beam spot diameter of 75 μm. The energy density was 10–11 J/$cm^2$ at a frequency of 20 Hz. The laser ablated material was then sent to the MC-ICP-MS with He as the carrier gas, and the U-Pb isotopes with very different mass numbers were received at the same time for the U-Pb measurement by expanding the dispersion with dynamic zoom adjustment. The laboratory internal standard AY-4 with the $^{206}Pb/^{238}U$ ID-TIMS age 158.2 ± 0.4 Ma was used as the measurement external standard. Every five cassiterite sample points were measured, and the standard samples were measured twice alternately to correct the analysis process and errors in the laser ablation process. The $^{206}Pb/^{207}Pb$-$^{238}U/^{207}Pb$ isochron method was used to correct ordinary lead in cassiterite at the same time (Hao et al., 2016; Cui et al., 2017). The ICPMSDataMSCal software of Liu et al. (2010) and Isoplot program of Ludwig (2003) were used for data processing and mapping.

Muscovite was extracted from the spodumene-bearing pegmatite from the Aktas Li deposit (sample HLT-1) and the 509 Li deposit (sample 509X-1) for Ar-Ar dating. Hand-picked grains were cleaned in de-ionised water and acetone. The samples were weighed and loaded into aluminium packets for irradiation. The packets were placed in a silicate glass tube (Can UM# 86), interleaved with packets containing the flux monitor Mount Dromedary Biotite (dated at 99.125 ± 0.076 Ma [0.077%]; Phillips et al., 2017). The canister was irradiated for 60 MWh (Mega Watt hours) at the CLICIT facility of the Oregon State University TRIGA reactor, United States.

After irradiation, the mineral separates were removed from their packaging and placed in tin foil packets. The $^{40}Ar/^{39}Ar$ step-heating analyses were carried out on a conventional double-vacuum Ta-resistance furnace attached to a VG3600 mass spectrometer with Daly and Faraday detector. Samples were outgassed at 450°C for 2 h. Following initial outgassing, aliquots were incrementally heating between 500° and 1350°C. It takes about 3 min to reach the desired temperature and the duration for each heating step was 20 min. The extracted gas was purified using multiple SAES Zr-Al getters before expansion into a VG3600 mass spectrometer. Extraction line blanks were measured before the analysis of each sample. After each sample analysis, the furnace was outgassed at 1500°C. High-temperature (1450°C) furnace blanks contained low levels of the measured isotopes and the blank corrections have a minimal impact on the measured data.

The mass discrimination and detector intercalibration were monitored by analysis of standard air volumes. The correction factors for interfering reactions, as determined by irradiation of high-purity K-glass and Ca-salt included in Can UM# 86, are indicated in the dataset, and the reported data have been corrected for system backgrounds, mass discrimination, fluence gradients, and atmospheric contamination, assuming the atmospheric argon composition of Lee et al. (2006). Unless otherwise stated, errors associated with the age determinations are one standard deviation and exclude uncertainties in the

**FIGURE 6 |** Geological map of the Dahongliutan area.
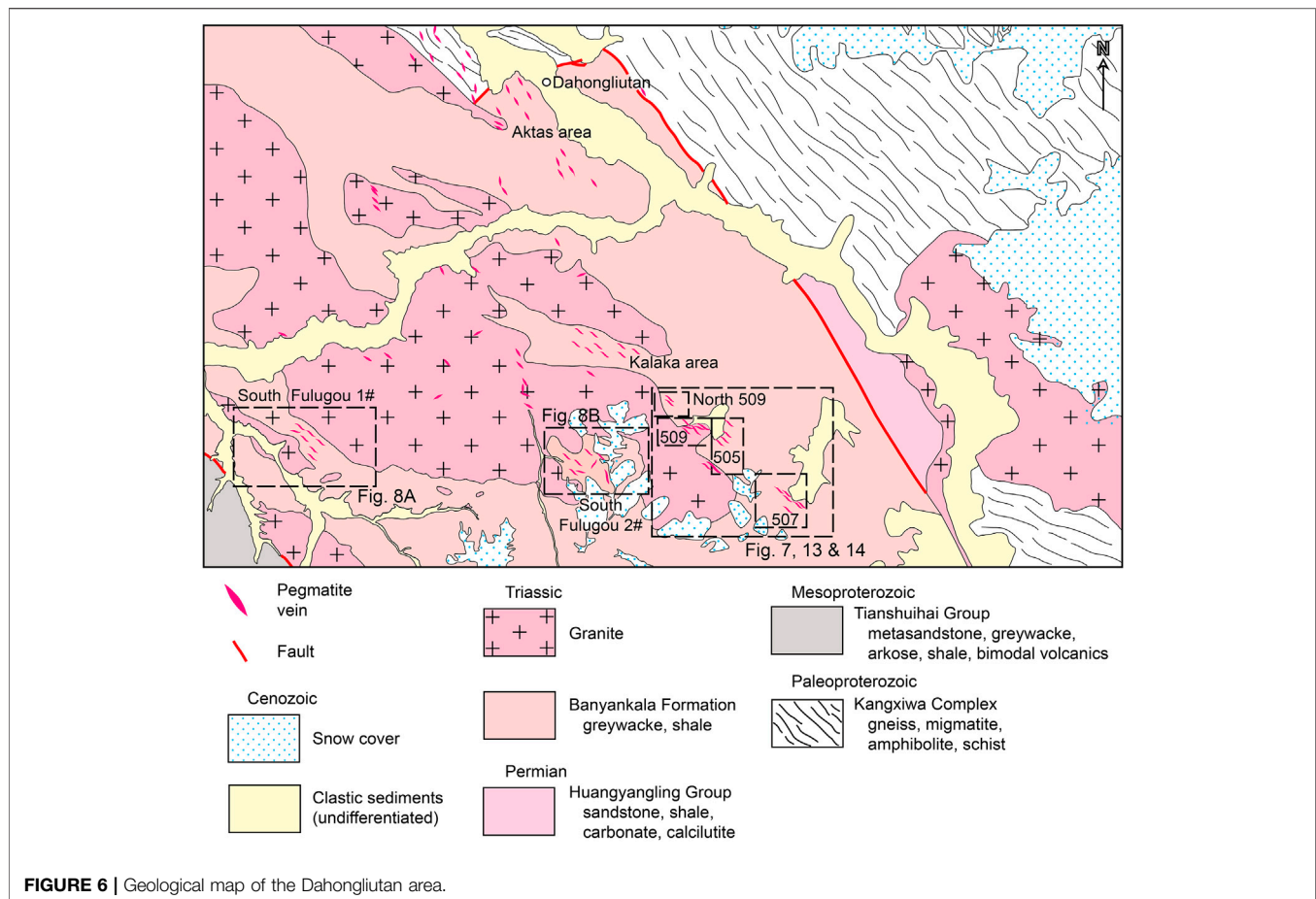
J-value, age of the fluence monitor and the decay constants. Ages have been calculated using the decay constants of Steiger and Jager (1977), and the $^{40}Ar/^{39}Ar$ dating technique is described in detail by McDougall and Harrison (1999).

## LITHIUM DEPOSITS DISCOVERED BY THIS STUDY

As outlined above, ore-bearing pegmatites have been delineated using a combination of remote sensing images, geological maps and geochemical anomalies, and were field checked following the procedure outline in **Figure 3**, which led to the discovery of the 505, 507, north 509, and South Fulugou 1# and 2# Li deposits (**Figure 6**). The $Li_2O$ grades of the anomalies are between 1.1 and 3.8%, based on the sampling of trenches and diamond-drillhole core, and the analyses indicate a combined resource of over 1.7 Mt $Li_2O$, but this is only an estimate given that exploration is still at an early stage. As a comparison, the Greenbushes deposit in Western Australia has an estimated contained Li resource of over 2.9 Mt $Li_2O$ (Geological Survey of Western Australia, Lithium Commodity Flyer, 2017).

## Geology of the Newly Discovered 505, 507, South Fulugou 1# and South Fulugou 2# Lithium Deposits

The 505 and 507 deposits are hosted by hornfelsed units of the Bayankala Formation near the contact with the southern part of the Dahongliutan Granite and have similar geological features as the 509 Li deposit (**Figure 7**). The Worldview-2 satellite images were used to interpret some of the pegmatite veins represented as NW-trending white hue and strip-like patterns and can be interpreted as sheeted veins (**Figure 4B**). The anomalies extracted using the ASTER sensing images were distributed at the contact with the Bayankala Formation and monzogranite (**Figure 4B'**).

The 505 deposit assays 0.02–0.04% BeO, 0.04–0.26% $Rb_2O$, and 0.02–0.04% (Nb + Ta)$_2O_5$, and the 507 deposit assays 0.02–0.05% BeO, 0.05–0.16% $Rb_2O$, and 0.01–0.02% (Nb + Ta)$_2O_5$. The exposed rocks at the 505 and 507 Li deposits are in the central and upper parts of the Bayankala Formation consisting of variably deformed grey to brown, thinly layered, and fine-grained feldspar-quartz sandstone interbedded with grey to black siltstone. The formation is cleaved subparallel to the NE-trending bedding. The beds are also folded plunging shallowly to moderately to the SE.

**FIGURE 7 |** Geological maps of the 505 Li deposit and 507 Li deposit.
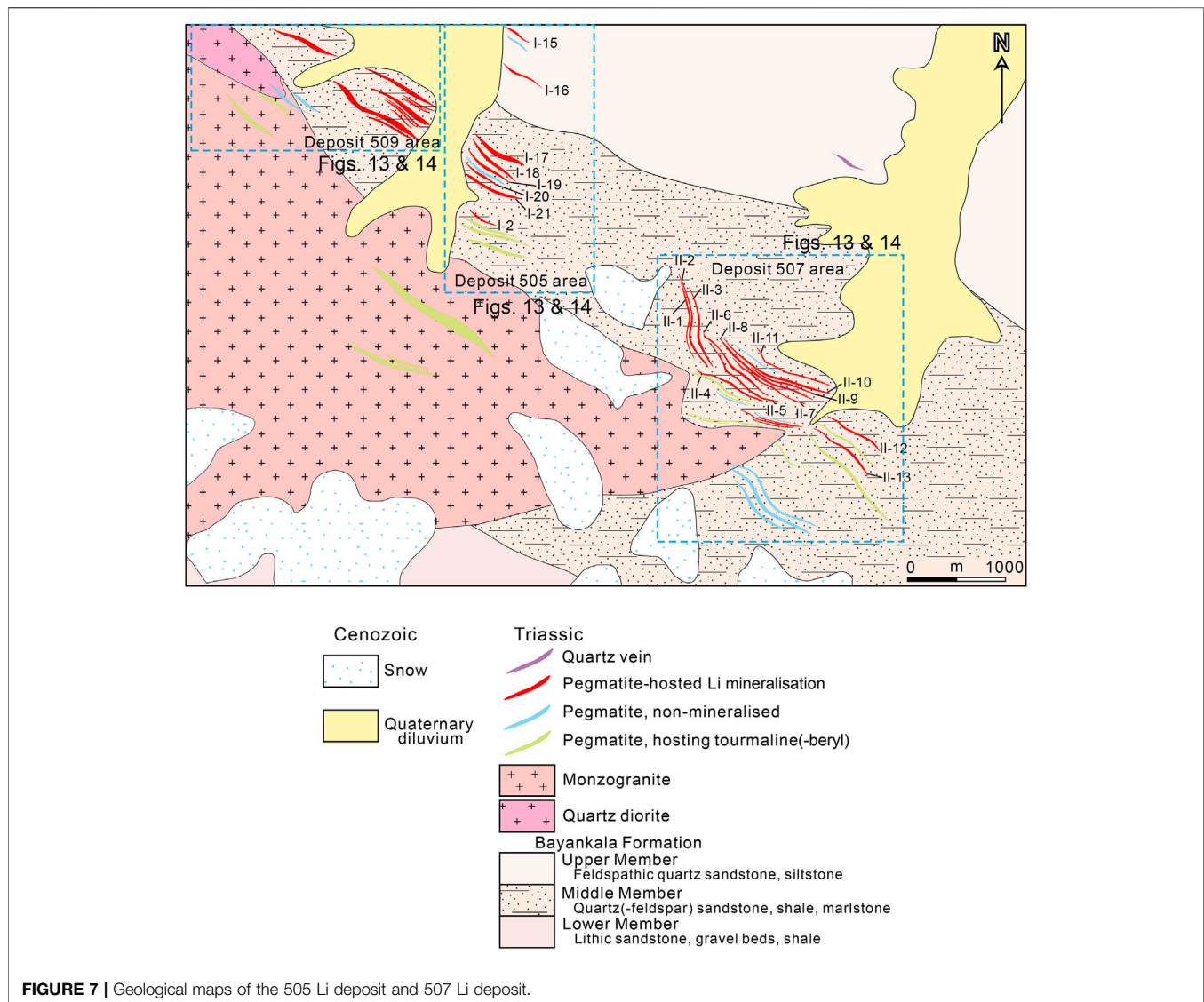
A total of 20 pegmatite veins were found at 505 forming 11 orebodies that are 1.5–4 m wide and 50–260 m long with an estimated Li resource is 0.01 Mt assaying 1.1–3.3% $Li_2O$ (**Supplementary Table S2**). Granodiorite and quartz diorite are present in the western part of the deposit intruding the Bayankala Formation. The contact alteration is up to 30 m wide and progresses from cordierite hornfels near the granite to andalusite hornfels further away. Some pegmatite veins were distributed at the contact zone.

The spodumene-pegmatite veins trend NW and parallel to the Qitaidaban Fault (**Figure 1B**), and are regionally zoned and are strongly associated with the andalusite-bearing hornfels (**Figures 10I,J**, **11**). The country rocks are brittle-ductile deformed and strongly cleaved, forming a series of lensoidal shears within the fault. The structure provides a good conduct for the pegmatite veins and associated mineralisation. Twenty-eight 300–1,200 m long and 1–9 m thick pegmatite veins were found at the 507 deposit, and 13 orebodies have been delineated. The orebodies

trend NW dipping moderately either to the northeast or southwest with an estimated resource of 0.44 Mt averaging 2.5% $Li_2O$ (**Supplementary Table S2**).

The South Fulugou pegmatite vein group is located on the south part of the Dahongliutan Granite where at least 110 pegmatite veins were highlighted on the satellite images. The central part of the group contains the South Fulugou 1# and 2# Li deposits, where the discovered mineralised pegmatites appear greyish to white on the satellite images. The mineralised pegmatite veins at South Fulugou 1# trend NW near the contact between the Dahongliutan Granite and Bayankala Formation in the western part of the study area (**Figure 8A**). Large shadows cast in valleys from adjoining mountains exist in the area on the Worldview-2 satellite images, making the accurate delineation of the pegmatite veins subtle (**Figure 4C**). The delineated remote sensing anomalies are in granite on the ASTER satellite images (**Figure 4C'**). The host rocks consist of greenschist to
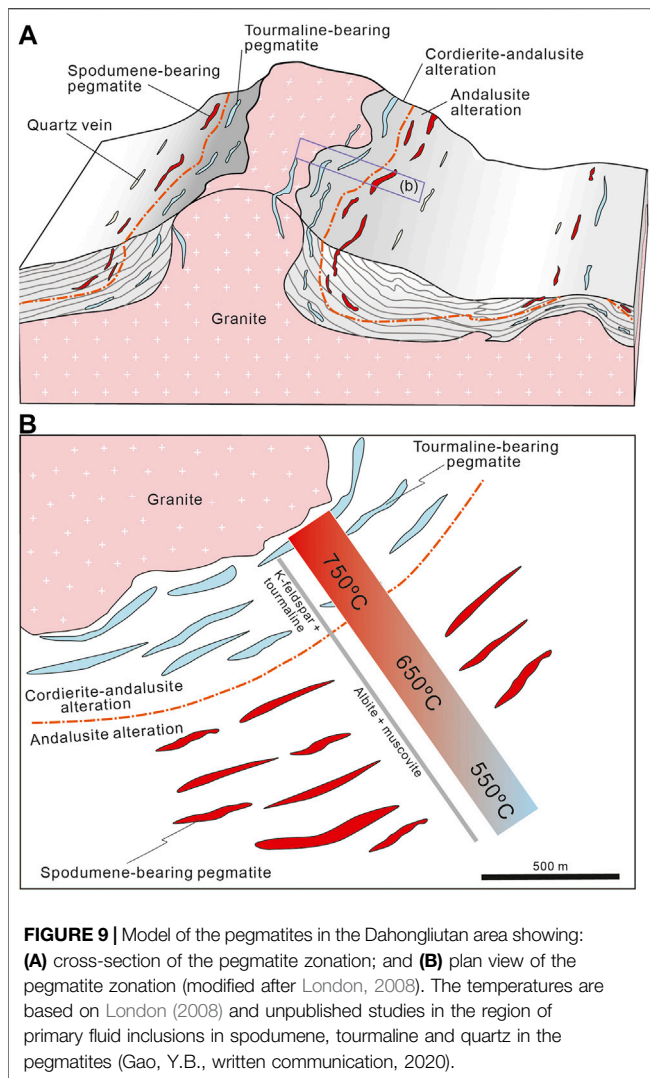
**FIGURE 8 |** Geological maps of: **(A)** the South Fulugou 1# Li deposit; and **(B)** the South Fulugou 2# Li deposit.
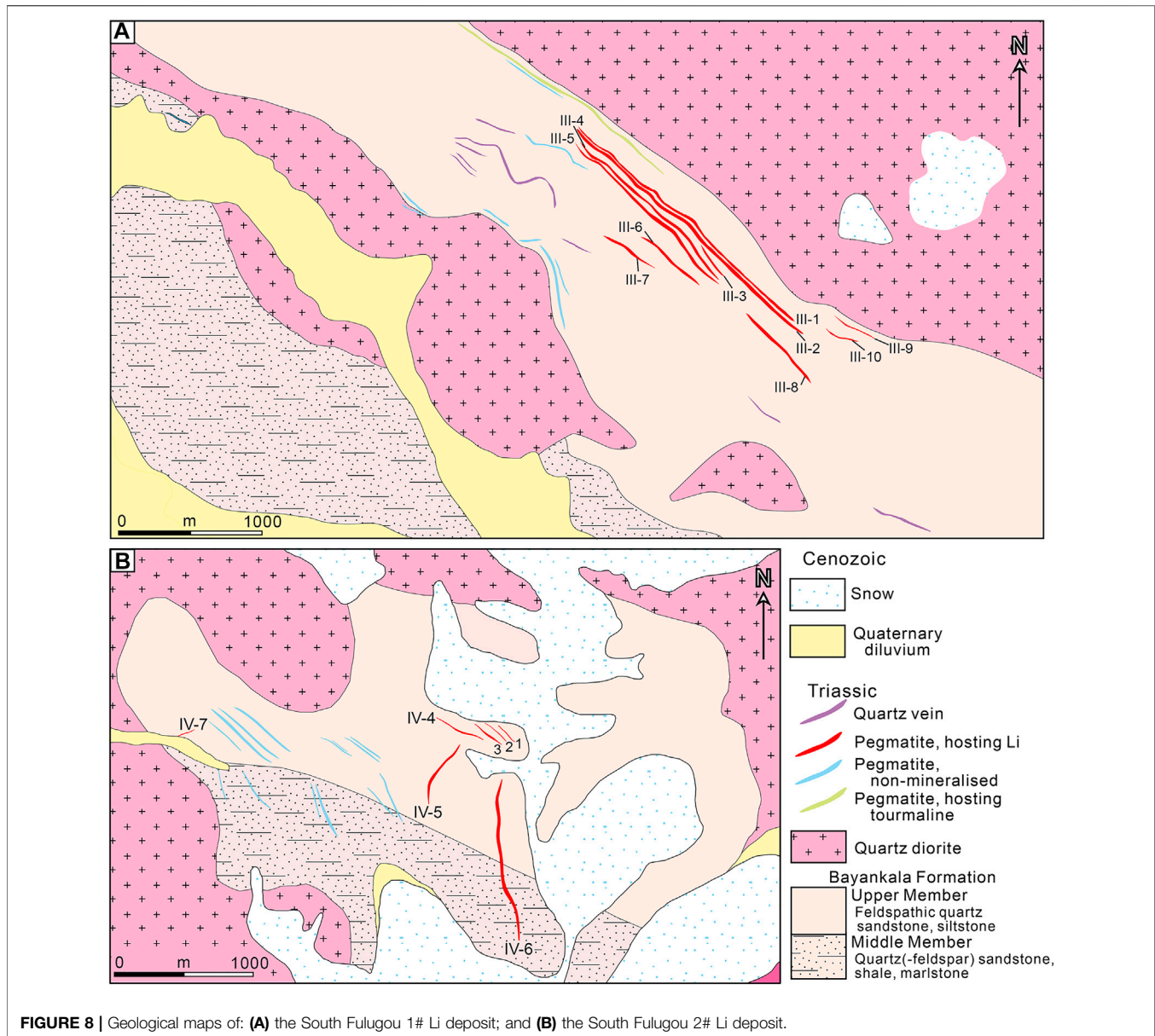
amphibolite facies light grey, fine-grained feldspar-quartz sandstone interbedded with grey, thinly layered siltstone, and biotite–quartz schist. The sequence dips moderately to the northeast (**Figure 8A**).

The exposed magmatic rocks include light grey to white, fine- to medium-grained and non-mineralised tonalite. There are two granitic outcrops in the area, which are located on the north and south sides of the Bayankala Formation. The country rocks progress from cordierite-andalusite hornfels, andalusite hornfels to sericite schist. The deposit is located of the northern limb of the South Dahongliutan antiform.

Twenty-one pegmatite veins were found in the South Fulugou 1# Li deposit hosted by the Bayankala Formation, and a small amount of pegmatite veins are present on the southern side of the

tonalite intrusion. The deposit includes ten lenticular Li orebodies dipping to the northeast subparallel to the layering (**Figure 8A**). The orebodies are up 18 m wide and up to 2,400 m long with an estimated resource is 0.58 Mt averaging 1.2–3.9% $Li_2O$, 0.03–0.08% BeO, 0.01–0.09% $Rb_2O$, and 0.01–0.02% $(Nb + Ta)_2O_5$ (**Supplementary Table S2**).

The South Fulugou 2# Li deposit is located at an elevation of 5,300–6,200 m to the east of the South Fulugou 1# deposit, west of the 509 Li deposit, and south of the Dahongliutan Granite (**Figure 4**). Both of the South Fulugou deposits are similar with pegmatite veins trending NW in the Bayankala Formation, although a small number of veins trend eastward. The pegmatites are represented by grey to while strips on the Worldview-2 satellite images (**Figure 4D**), and the delineated

FIGURE 9 | Model of the pegmatites in the Dahongliutan area showing: (A) cross-section of the pegmatite zonation; and (B) plan view of the pegmatite zonation (modified after London, 2008). The temperatures are based on London (2008) and unpublished studies in the region of primary fluid inclusions in spodumene, tourmaline and quartz in the pegmatites (Gao, Y.B., written communication, 2020).

ASTER remote sensing anomalies are distributed within the granite (**Figure 4D'**).

The South Fulugou 2# deposit has an estimated resource of 0.14 Mt averaging 0.9–2.6% $Li_2O$, 0.02–0.05% BeO, 0.04–0.34% $Rb_2O$, and 0.01–0.02% $(Nb + Ta)_2O_5$ (**Supplementary Table S2**) (**Figure 8B**). The deposit is hosted by the Bayankala Formation that consists of thinly layered, metamorphosed, fine-grained feldspar-quartz(-garnet-sericite) sandstone and light grey biotite-quartz schist. Light grey, fine-to medium-grained quartz diorite is exposed to the east, west, and north of the deposit. The diorite contains mafic xenocrysts and is locally foliated in biotite forming a gneissic texture. The deposit contains seven mineralised pegmatite veins (**Figure 8B**), which are 120–1,100 m long and 2–12 m wide. In addition, a ~680 m long and 2 m wide mineralised pegmatite vein is present in faulted quartz diorite at the western part of the deposit, where the vein dips shallowly towards the NE. This contact relationship is rarely exposed, but where exposed shows that the pegmatite is younger than the quartz-diorite.

## Pegmatite Zonation

The kinds of granitic pegmatites present are spodumene-bearing, and tourmaline-bearing. The composition of the pegmatite veins change from quartz-K-feldspar-tourmaline(-muscovite) proximal to the Dahongliutan Granite to spodumene-bearing plagioclase-quartz-muscovite(-microcline-garnet) distal from the granite (**Figure 9**). The spodumene-bearing pegmatite veins are present 200–1,500 m from the Dahongliutan Granite in the Bayankala Formation (**Figures 10A** and **9**). The veins trend NW, dip moderately to steeply NE and their location is structurally controlled by joints and shears (**Figures 10B,C**). The spodumene is grey, up to 0.15 m long (larger than other minerals in the veins), and constitute between 5 and 30% of the veins, although the highest content can reach 70% of the veins (**Figure 10D–F**). The veins are small and not commonly zoned, and where present contains baren edges and mineralised cores containing spodumene as the Li-bearing mineral. The location of the mapped mineralised pegmatite veins are shown in **Figures 6**, **7**, **8**.

The tourmaline-bearing pegmatites contain long columnar or needle-shaped black tourmaline with spherical, triangular or banded cross-sections, and are orientated perpendicular to the pegmatite vein (**Figure 10G**). The pegmatites in the Dahongliutan Granite contain quartz occupying spaces between K-feldspar and muscovite (**Figure 10H**). Also present are jointed, lenticular quartz-muscovite veins that cut the spodumene-bearing pegmatites and trend subparallel and oblique to the metasedimentary host rocks (**Figure 10E–I**). The metasedimentary rocks near the Dahongliutan Granite are strongly hornfelsed containing cordierite and andalusite near the granite progressing outward to andalusite and sericite-rich hornfels at the edge of the contact metamorphism. The spodumene-bearing pegmatites are not internally zoned and are strongly associated with the andalusite-bearing hornfels (**Figure 10M,N**).

Several types of pegmatites are presented in the area that include massive, patchy, and dendritic textures. The massive texture is fine-to medium-grained monoclinic, although two or more minerals can be massive in the form of banding and seriate textures. The long axis of the spodumene and tourmaline are lineated perpendicular to the strike of the pegmatite veins. The patchy texture is characterised by minerals such as spodumene, quartz, plagioclase, and sodium plagioclase with different grain sizes. The dendritic texture is common in the mineralised pegmatites and characterised by elongated and wedge-shaped dendritic crystals including spodumene-niobium-tantalum minerals, cassiterite, and triphylite $(LiFePO_4)$ in feldspar and quartz. The association of Li-Nb-Ta-Sn in these pegmatites places them in the Li-Cs-Ta (LCT) - type, as defined by Cerný and Ercit (2005).

The main ore mineral is grey-white to green spodumene with lesser amounts of amblygonite $(Li,Na)AlPO_4(F,OH)$, lithium muscovite, beryl, and niobite also known as columbite $((Fe, Mn)Nb_2O_6)$. The spodumene is idiomorphic, fine-to coarse-grained and is larger than other minerals in the pegmatite (**Figures 11A,B**). The long axis is between 30 and 150 mm,

**FIGURE 10** | Photographs of rocks in the Dahongliutan area: **(A)** spodumene-bearing pegmatite intruding meta-sandstone in the Bayankala Formation; **(B)** spodumene-bearing pegmatite subparallel to layering in the host rocks; **(C)** an example of spodumene-bearing pegmatite cross-cutting layering in the country rocks; **(D)** long, grey to white spodumene crystals intergrown with muscovite and quartz hosted by a fault; **(E)** pegmatite consisting of muscovite, albite, quartz, and spodumene;**(F)** green rubellite (tourmaline) coexisting with spodumene in pegmatite; **(G)** tourmaline-bearing pegmatite consisting of black tourmaline, plagioclase, muscoviteand quartz; **(H)** non-mineralised pegmatite consisting of plagioclase, muscovite and quartz; **(I)** an example of quartz veining in meta-sandstone; **(J)** hornfelsed greysiltstone containing cordierite; **(K)** dark grey andalusite in hornfelsed siltstone; and **(L)** garnet-bearing hornfelsed siltstone located near a spodumene-bearing pegmatite.Zoned pegmatite dykes in the Dahongliutan area containing: **(M)** black tourmaline-plagioclase-muscovite-quartz, plagioclase-quartz-muscovite, and quartz-muscoviteplagioclase; and **(N)** quartz-muscovite-plagioclase, and spodumene-quartz-albite-muscovite. Abbreviations: Spd, spodumene; Qtz, quartz; Ms, muscovite; Pl, plagioclase; Ab, albite; Tur, tourmaline.
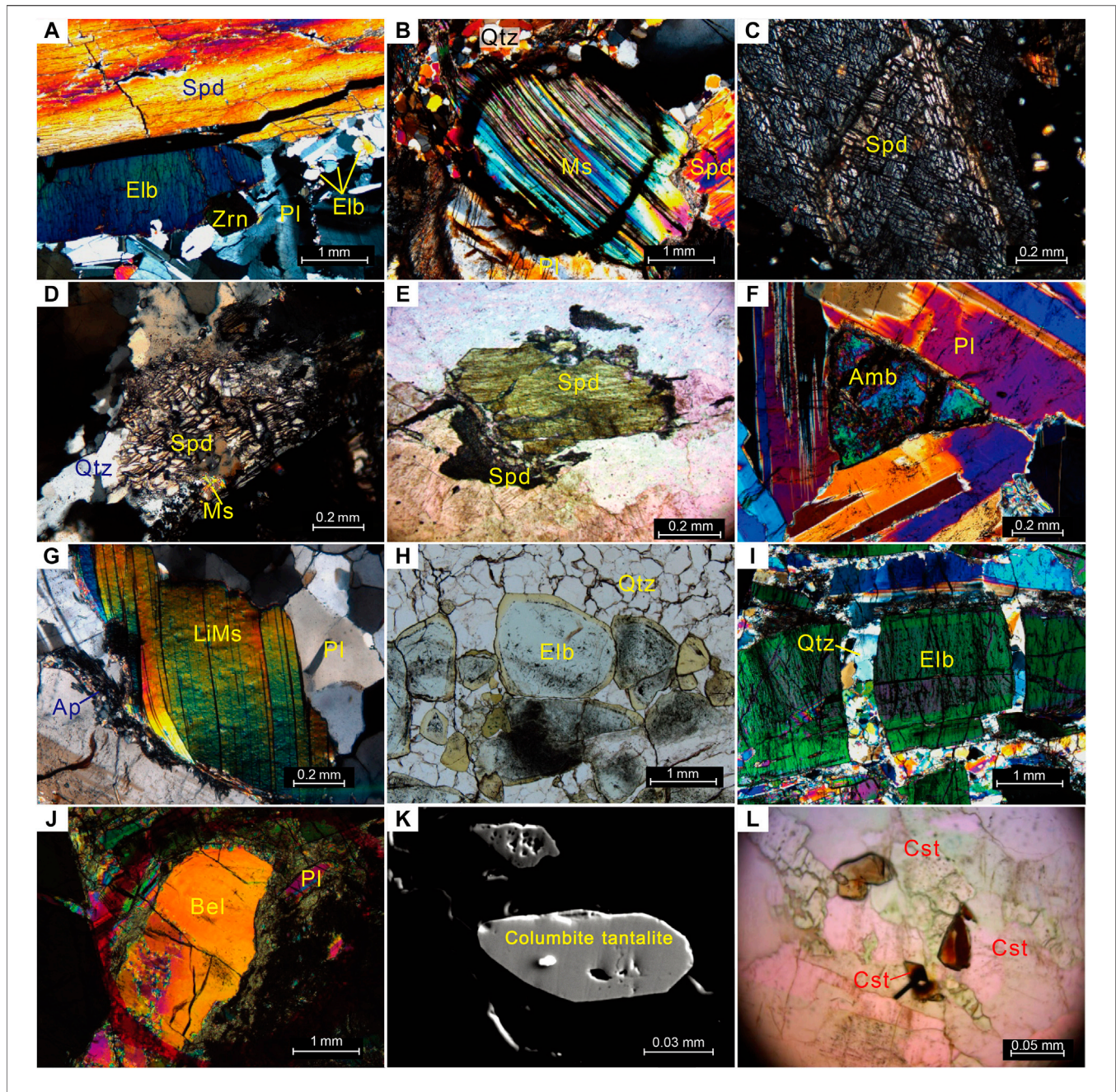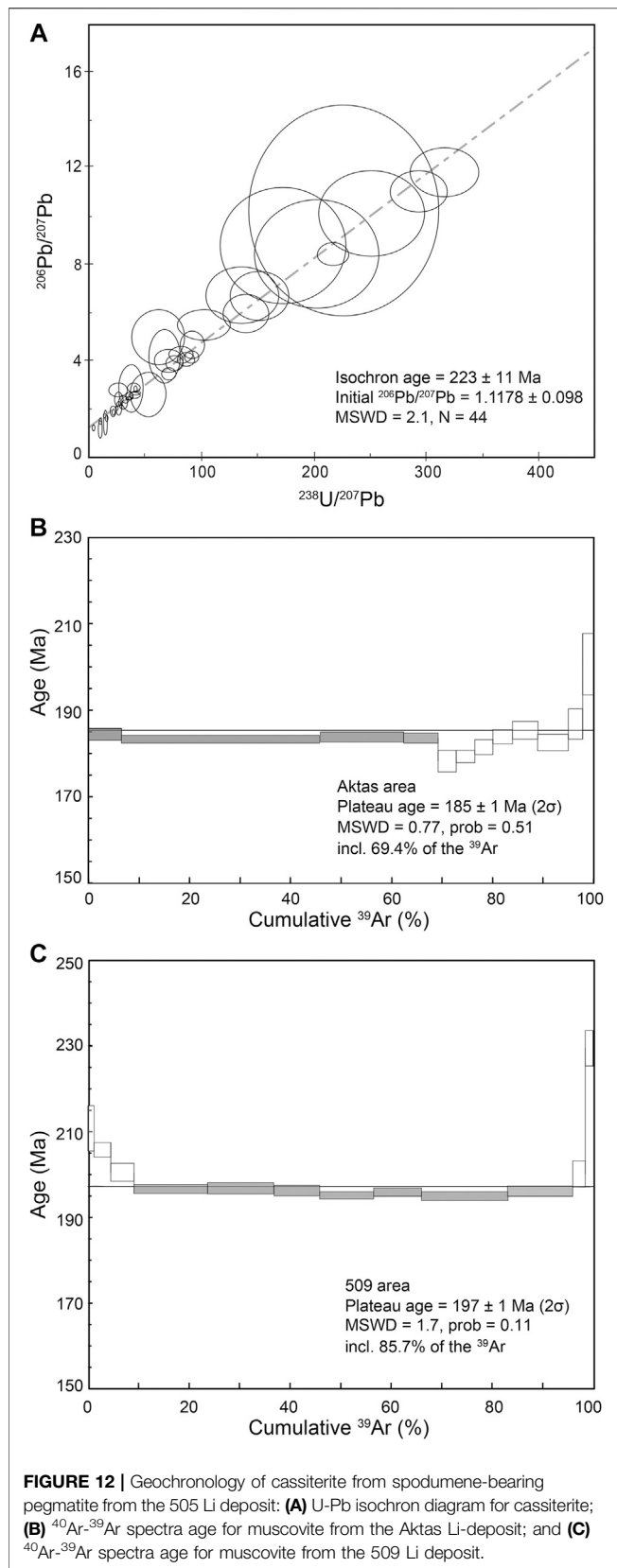
**FIGURE 11 |** Photomicrographs of samples from the Dahongliutan area showing: **(A)** example of spodumene-bearing pegmatite containing, elbaite, plagioclase and minor zircon; **(B)** spodumene-bearing pegmatite dykes consisting of muscovite, plagioclase and quartz; **(C)** cleaved spodumene; **(D)** quartz and muscovite filling fractures in spodumene; **(E)** late fibrous spodumene crystallised on the edge of early columnar spodumene; **(F)** a small amount of 0.2 -1 mm wide allomorphic and granular amblygonite associated with spodumene and plagioclase; **(G)** lithium-bearing, 1 and 5 mm long muscovite with a low and high refractive index; **(H)** two forms of light green elbaite; **(I)** dark green and columnar elbaite crossed by quartz and muscovite; **(J)** example of rare beryl; **(K)** back-scatter electron (BSE) image of tabular, 0.04 -0.20 mm long irregular and granular columbite-tantalite with a semi metallic luster; and **(L)** semi-automorphic to allomorphic granular 0.1 and 0.2 mm long cassiterite associated with the early spodumene. Abbreviations: Spd, spodumene; Qtz, quartz; Ms, muscovite; LiMs, lithium-bearing muscovite; Pl, plagioclase; Ab, albite; Amb, amblygonite; Zrn, zircon; Ap, apatite; Tur, tourmaline; Elb, elbaite; Bel, beryl; Cst, cassiterite.

and has cleavage orientated in two directions at close to right angles (**Figure 11C**). Partings within the spodumene are locally filled by quartz and muscovite veining, showing that the quartz-muscovite veins are late in the paragenesis of the veining

(**Figure 11D**). Furthermore, hair-like spodumene is also present along the edge of idiomorphic spodumene exists at the edge of the pore-existing spodumene, showing that there are two spodumene generations (**Figure 11E**).

**FIGURE 12** | Geochronology of cassiterite from spodumene-bearing pegmatite from the 505 Li deposit: **(A)** U-Pb isochron diagram for cassiterite; **(B)** $^{40}$Ar-$^{39}$Ar spectra age for muscovite from the Aktas Li-deposit; and **(C)** $^{40}$Ar-$^{39}$Ar spectra age for muscovite from the 509 Li deposit.

The amblygonite in the mineralised pegmatite is 0.2–1 mm across, and it is often associated with spodumene and albite, and the lithium muscovite ranges from 2 to 5 mm long (**Figure 11F–G**). The spherical triangle of elbaite (Na(Li1.5Al1.5)Al6Si6O18(BO3)3(OH)4) is observed in cross section, with cracks were filled by later quartz and mica (**Figure 11H–I**). The beryl is rare, and the columbite-tantalite crystals are between 0.04 and 0.2 mm across (**Figure 11J–K**). The cassiterite is typically hypidiomorphic (**Figure 11L**), with a grain size of 0.1–0.2 mm. It is associated with the early spodumene, and some columbite and columbite-tantalite crystals are 0.04–0.2 mm long and co-existing cassiterite.

## Age of the Lithium Mineralisation

Cassiterite co-existing with spodumene was collected from the 505 deposit for dating. The LA-MC-ICP-MS cassiterite U-Pb dating obtained 44 valid points (**Supplementary Table S3**). The $^{238}$U/$^{207}$Pb ratio is between 3.388 and 315.89, the $^{238}$U/$^{206}$Pb ratio ranges from 2.864 to 28.758, and the $^{206}$Pb/$^{207}$Pb value is 1.159–11.837. The $^{206}$Pb/$^{207}$Pb-$^{238}$U/$^{207}$Pb isochron age is 223 ± 11 Ma (MSWD = 2.1) (**Figure 12A**).

Sample HLT-1 of primary muscovite co-existing with spodumene from Aktas was analysed using 12 stages with $^{40}$Ar/$^{39}$Ar step-by-step heating experiments from 650° to 1,450°C (**Supplementary Table S4**). A relatively flat plateau age of 185 ± 1 Ma formed during the temperature stage from 650° to 800°C (**Figure 12B**), including 69.4% of the released $^{39}$Ar. Sample 509X-1 of primary muscovite co-existing with spodumene from the 509 deposit was also analysed using 12-stages $^{40}$Ar/$^{39}$Ar step-by-step heating experiments from 650° to 1,450°C, and a relatively flat plateau age of 197 ± 1 Ma formed during temperature stage from 730° to 1,050°C (**Figure 12C**), including 85.7% of the released $^{39}$Ar.

## DISCUSSION

### The Rapid Exploration Method Using Remote Sensing Data

As mentioned earlier, spectroscopic tests show that the spodumene-bearing pegmatite exhibits strong absorption (~2,200 nm), second-order absorption (~2,350 nm), and reflection characteristics (~560 and 760 nm). The absorption and reflection characteristics correspond to each band of remote sensing images originating from Worldview-2 and ASTER data. The spodumene-bearing pegmatite veins and dykes display reflection in B4 of the Worldview-2 data, and B4 and B2 of the ASTER data. In addition, the spodumene-bearing pegmatites display strong absorption in the ASTER B5 and secondary absorption in the ASTER B8 data. Based on these characteristics of the pegmatites, the principal component transformation method is used to extract remote sensing anomalies related to rare metal concentrations. Most of the Li mineralisation, however, was discovered at the periphery of
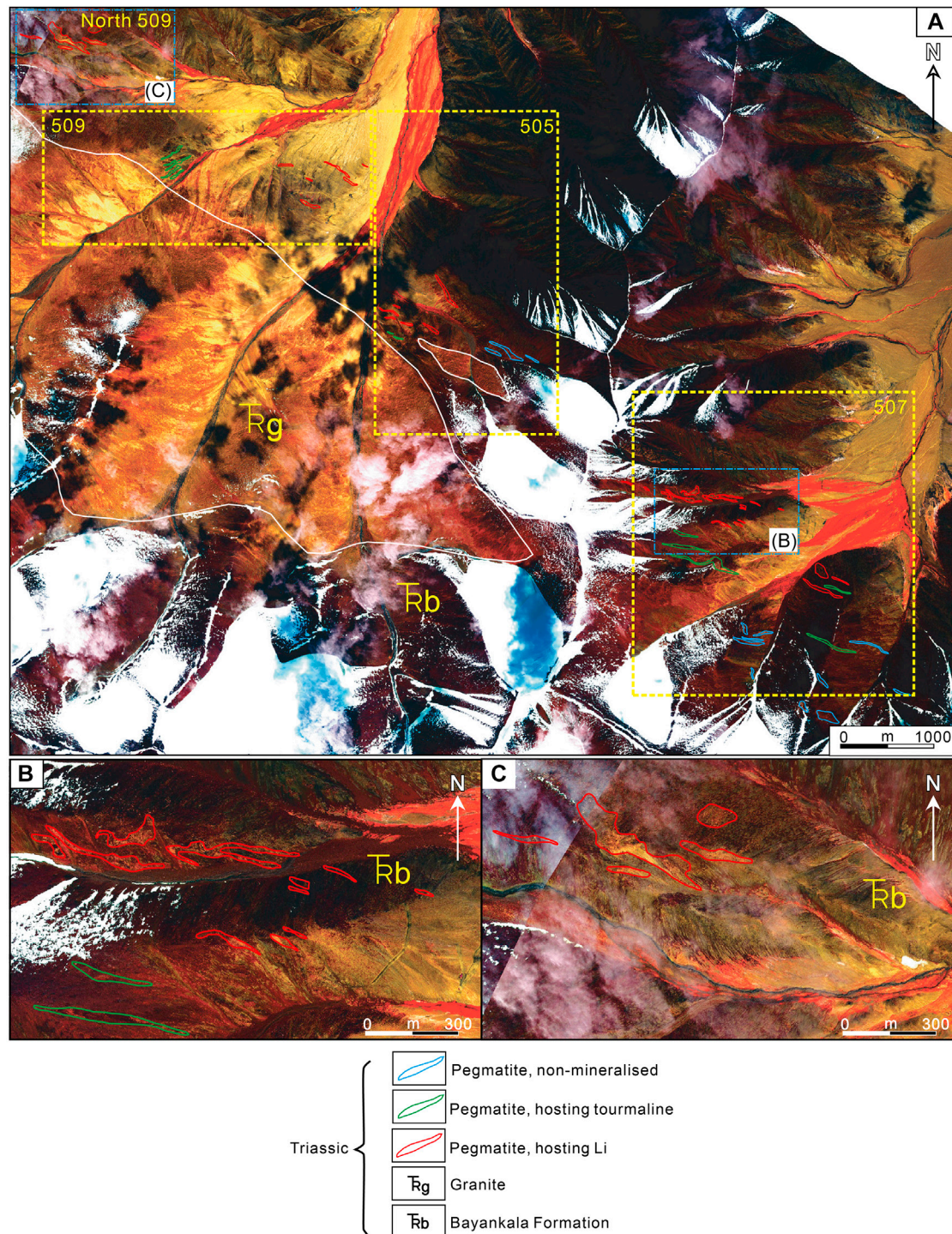
**FIGURE 13 |** Worldview-3 remote sensing images with an 841-band combination and enhanced processing for the 505, 507 Li deposits and surrounding areas showing: **(A)** the whole area; **(B)** the 507 Li-deposit; and **(C)** the potential area for Li deposits in the North 509 area. Pegmatite veins with widths of at least 1 m appear white on the images and the Bayankala Formation host is red and greyish brown in colour in parts **(B, C)**. The increased resolution of the Worldview-3 images resulted in an increase in the recognition of mineralised pegmatite dykes in part **14C**.

remote sensing anomalies. Furthermore, given that the resolution of the ASTER images is 15 m, the spodumene-bearing pegmatite display mixed pixels on the ASTER remote sensing images,

making it difficult to accurately pin-point the location of these pegmatites that are commonly less than 15 m wide. This is also limited by the Sentinel-2, Landsat-5 and Landsat-8 images
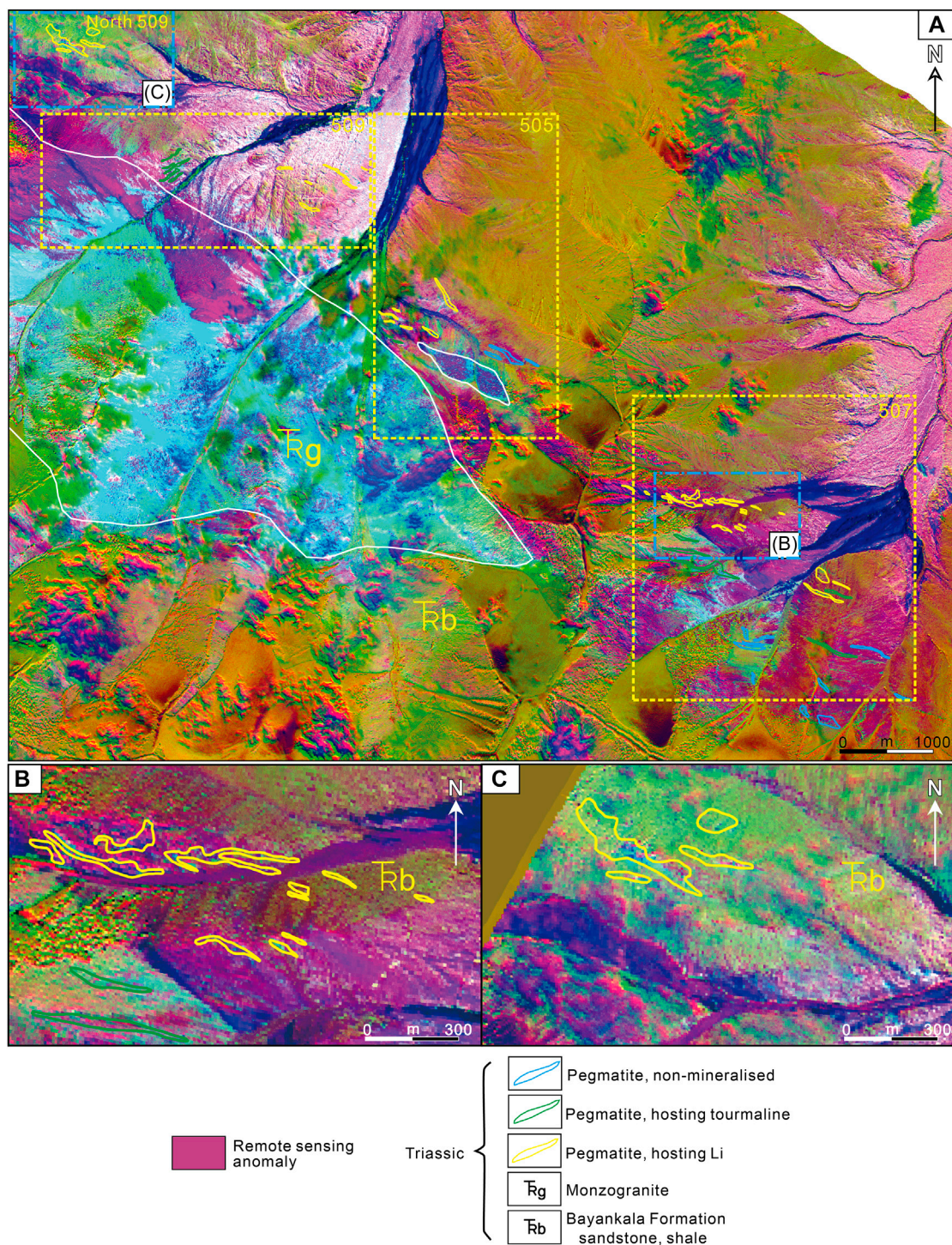
**FIGURE 14 |** Worldview-3 Remote sensing anomalies in the 505 and 507 Li deposits and surrounding areas: **(A)** the whole area; **(B)** the 507 Li deposit; and **(C)** the potential area for Li mineralisation in the North 509 area.

(Mendes et al., 2017; Cardoso-Fernandes et al., 2018; Cardoso-Fernandes et al., 2019a). In contrast, the location of pegmatites less than 1 m wide can be recognised using high-resolution Worldview-2 images. The ASTER images highlight the presence of muscovite enriched in pegmatites, granitic rocks, and the widespread hydrothermal alteration around spodumene-bearing pegmatites at a metre-scale. The alteration is the result of the subsolidus reactions with residual pegmatitic fluid.

Consequently, the combination of Worldview-2 and ASTER images forms a key tool in discovering mineral occurrences, especially in the West Kunlun and Karakoram regions where more rocks are exposed. The application of this exploration method in the mountainous Dahongliutan area of the Bayankala Fold Belt has led to the discovery of large Li deposits at the 505, 507, South Fulugou 1#, and 2# deposits.

It is emphasised that the newly launched Worldview-3 remote sensing satellite has 16 bands. The spectrum range includes visible light to short-wave infrared. The spatial resolution of the visible light to near-infrared is 0.3 m and short-wave infrared is 3.7 m. It solves the shortcomings of the low spatial resolution images developed from the ASTER data, and the narrow spectral range available from the Worldview-2 data. Thus, the Worldview-3 enhanced remote sensors potentially make easier to recognise the location of pegmatite veins.

New Worldview-3 remote sensing images were adopted with an 8-4-1 band combination and enhanced processing for the 505 and 507 Li deposits and surrounding areas (**Figure 13A**). Pegmatite veins with widths of at least 1 m appear white on the images and the Bayankala Formation is red and greyish brown in colour (**Figures 13A,B**). The increased resolution of the Worldview-3 images resulted in an increase in the recognition of mineralised pegmatite dykes (**Figure 13C**). Four principal components (PC 1–4) were obtained by applying the principal component transformation of four bands (B1, B2, B14 and B16) from the Worldview-3 images. The PC3, PC4 and PC1 principal components were used to generate RGB pseudo-colour synthesis, which is a multi-band monochromatic image combination. The PC4 principal component and rare metal mineral mineralisation presents high values in the transformed image, which is obviously different from the values corresponding to granite and supracrustal wallrocks (**Figure 14A**). The false colour image for the host granite is blue area, the metasedimentary wall rocks appear as yellow-green, and the Li-bearing pegmatites are marked by a purple-red colour, which is located outside the contact zone (**Figures 14A,B**). These criteria were used north of the 509 Li deposit highlighting the potential areas for Li mineralisation (**Figure 14C**). Lithium-bearing pegmatites were also found during geological mapping and exploration trenching. As a result, a Li resource of 0.5 Mt averaging 1.7% $Li_2O$, 0.05% BeO, 0.25% $Rb_2O$, 0.027% $(Nb + Ta)_2O_5$ and 0.065% $Cs_2O$ have been found. The largest mineralised pegmatite is 1,140 m long and 58 m wide.

## Interpretation of the Cassiterite U-Pb and Muscovite $^{40}Ar/^{39}Ar$ Ages

Our LA-MC-ICP-MS cassiterite U-Pb and $^{40}Ar/^{39}Ar$ muscovite dating of cassiterite and muscovite associated with spodumene show that the mineralisation is between ca. 223 and 185 Ma. Given the Ar-Ar date corresponds to the muscovite's closure temperature of ~425°C (Harrison et al., 2009), the ca. 185 Ma date is the lowest age limit, and the ca. 223 Ma (Late Triassic) date is closest to the age of the mineralisation. It can be suggested from these dates that the metamorphism associated with the

emplacement of the granite, lasted for 40 million years. The regional implications of the ca. 223 Ma age of the granitic pegmatites are discussed below.

## Tectonic Setting and Resource Potential

The regional Triassic granites are distributed on the north and south sides of the Kangxiwa Fault in the West Kunlun Orogen, and the Tashkurgan and Tianshuihai terranes (**Figure 1**). The genesis of the granites are thought to be related to subduction and closure of the Paleo-Tethys Oceanic Plate, with the ca. 228 Ma granite in the Kudi area being emplaced in the suture between the West Kunlun Orogen and Tashkurgan-Tianshuihai terranes during late orogenesis (Jiang and Yang, 2000). The age of the protolith for the gneissic granite at the Bulunkou village at the northern edge of Western Kunlun Orogen is 241 ± 2 Ma, which is interpreted as being emplaced in a compressional setting (Zhang et al., 2005). A younger (228 ± 1 Ma) amphibole-bearing monzogranite located about 400 km to the southeast near the Kudi Village is interpreted as being emplaced in an extension setting following the collision between the South Kunlun and Tianshuihai terranes (Zhang et al., 2005).

Jiang et al. (2013) propose that the Paleo-Tethys Oceanic Plate subducted northward during ca. 338 to 251 Ma, and the South Kunlun Terrane collided with the Tianshuihai Terrane at ca. 243 Ma. This was followed by the emplacement of high-K calc-alkaline granites during ca. 234–227 Ma (Jiang et al., 2013). Yang (2013) proposes that the subduction of the oceanic crust during ca. 251 Ma was followed by continent-continent collision during ca. 242 Ma, and over-thickening of the continental-crust during ca. 231–223 Ma. This was succeeded by post-collisional extension and the emplaced of granites during ca. 215–185 Ma. The non-mineralised pegmatite veins and dykes in the Dahongliutan area were emplaced during ca. 224–218 Ma (Liang et al., 2019), and the spodumene-bearing pegmatite veins were emplaced during ca. 223–209 Ma (Qiao et al., 2015; Wei et al., 2017; Yan et al., 2018; Wang et al., 2020). This latter age is consistent with the age of granites being emplaced during a post-collisional extension between the South Kunlun and Tianshuihai terranes (c.f. Qiao et al., 2015; Wei et al., 2017; Zhang et al., 2018). Based on the geological constraints discussed above, we propose that the LCT-type pegmatite veins and dykes in the Dahongliutan area originate from fractionating granites during a ca. 223 Ma post-collisional extensional setting.

The understanding of the orogenesis of the Dahongliutan Granite and its associated Li mineralisation is at an early stage and requires further studies. It is currently proposed that the Dahongliutan mineralised pegmatites are genetically associated with the Triassic Dahongliutan Granite, and the regional zonation of the pegmatites around the granite (**Figures 6–9**). The zonation is related to mineral fractionation from the parental magma, as mentioned above. These characteristics are similar to the classical model of a zoned LCT-type deposit (Černý, 1989), which is consistent with the Dahongliutan pegmatite dykes and veins evolving from highly fractionated granitic magma (Wang et al., 2020). The crystal fractionation leads to progressive enrichment of incompatible ore-forming elements and volatile components, such as Li, Rb, Be, Cs, P, Cl, and F in

the residual fluid or melt (Thomas and Davidson, 2016). The high-volatility content of a magma can reduce its viscosity and liquidus temperature (Baker and Vaillancourt, 1995), which further delays the crystallisation of the evolved magma explaining the presence of the regional zonation of the Dahongliutan Granite (Mulja and Williams-Jones, 2018). The crystal-fluid interaction in the Li-mineralised pegmatites' parental magma related to a closed magmatic-hydrothermal system (Fan et al., 2020). This led to the final precipitation of spodumene associated with cassiterite and muscovite, which we dated. The widespread Li mineralisation in the Dahongliutan area can be compared to the giant Yajiang-Maerkang Li deposits in the Songpan-Ganzi Orogen in China (Xu et al., 2018). The Li deposits at Dahongliutan also compares closely to the Jiajika Li deposit in western Sichuan Province in terms of its geological setting, age (ca. 223–216 Ma,), and country rocks (Hao et al., 2015; Liu et al., 2015).

The newly discovered Li deposits in the Dahongliutan area are along the edges and southeastern exposures of Triassic granites, but the intervening mountainous areas that are difficult to explore are here regarded as having high prospectivity. An analogue is the No. X03 orebody at the Jiajika Li deposit that bifurcates and thickens in places, where lamellar and lenticular spodumene-bearing pegmatites extend at depth following the hornfels bordering the associated granite (Fu et al., 2015).

The remote sensing interpretation of the distribution of pegmatite veins on a regional scale shows that many pegmatite veins are present in areas such as the Kangxiwa-Aksayi River north of Dahongliutan where muscovite alteration is extensive. Furthermore, some late Triassic pegmatite veins contain beryllium, niobium, and tantalum mineralisation (Zhang et al., 2019). Thus, the Dahongliutan Li-mineralised area has potential for Be, Nb, and Ta deposits.

## CONCLUSIONS

Remote sensing accompanied by fieldwork and geochemistry are the main focus of this manuscript. This led to the discovery of mineralised pegmatites in the Dahongliutan area at a high altitude. The mineralised are classified as the LCT-type and interpreted as being relating to granitic fractionation. The distribution of the pegmatites in the area is structurally controlled by joints and shears within the Bayankala Formation and Dahongliutan Granite. The spodumene-bearing pegmatite dykes and veins are located broadly between tourmaline-bearing pegmatites near granites, and feldspar-rich pegmatites and quartz veining outside the contact hornfels zone. The spodumene-bearing pegmatite dykes and veins are associated with relatively elevated assays of Be, Rb, Nb and Ta.

The LA-MC-ICP–MS $^{206}Pb/^{207}Pb$-$^{238}U/^{207}Pb$ isochronal age of 223 ± 11 Ma for cassiterite from the spodumene-bearing pegmatite shows that the pegmatites in the Kangxiwa-Dahongliutan area are Late Triassic in age. The date also shows that the pegmatites were emplaced in a post-collisional extensional setting coeval with the age of the Dahongliutan Granite (indicating a probable genetic relationship between the granite and pegmatite veins). The $^{40}Ar/^{39}Ar$ plateau age of 197 ± 1 to 185 ± 1 Ma for muscovite from the mineralised pegmatite is interpreted as the minimum age of the hydrothermal alteration.

The exploration strategy developed for locating spodumene-bearing pegmatites in the rugged Bayankala Fold Belt includes the recognition of Li-bearing pegmatites in sedimentary horizons. This was followed by the identification of pegmatite veins on high-resolution hyperspectral remote sensing images and anomalies related to pegmatite-type Li deposits using multispectral remote sensing images. The metre-wide Li-bearing pegmatites in the study area are associated with rare metal geochemical anomalies, as determined from the geochemistry of rock samples from trenches and diamond-drillhole core.

The method established for the Dahongliutan area proved successful in discovering several significant Li and Be deposits in the region, such as 505, 507, north 509, South Fulugou 1#, and 2#. This new technique incorporating geological mapping, geochemistry and interpretation of high-resolution remote sensing has proven to be an important breakthrough for the rapid discovery of pegmatite deposits in the rugged West Kunlun and Karakoram terrains of China. This exploration method can be also developed in the areas with good outcrops and less rugged terrains. Finally, there is now a significant potential for identifying the location of Li-bearing pegmatites using hyperspectral remote sensing with a better spatial and spectral resolution.

## DATA AVAILABILITY STATEMENT

The original contributions presented in the study are included in the article/**Supplementary Material**, further inquiries can be directed to the corresponding author.

## AUTHOR CONTRIBUTIONS

YG, LB, KL, and MJ contributed to the conception and design of the study. YG wrote the first draft of the manuscript and led the data analysis and interpreted the results with LB, MJ, YL, and JT. All authors contributed to manuscript revision, read and approved it for publication.

## FUNDING

# ACKNOWLEDGMENTS

# REFERENCES

Baker, D. R., and Vaillancourt, J. (1995). The low viscosities of F+H$_2$O-bearing granitic melts and implications for melt extraction and transport. *Earth Planet Sci. Lett.* 132, 199–211. doi:10.1016/0012-821x(95)00054-g

Bedini, E. (2011). Mineral mapping in the Kap Simpson complex, central East Greenland, using HyMap and ASTER remote sensing data. *Adv. Space Res.* 47 (1), 60–73. doi:10.1016/j.asr.2010.08.021

Cao, R., Gao, Y. B., Chen, B., Bagas, L., Yan, S. C., Zhao, H., et al. (Forthcoming 2020). Pegmatite magmatic evolution and rare metal mineralisation of the Dahongliutan pegmatite field, Western Kunlun Orogen: constraints from the B isotopic composition and mineral-chemistry. *International Geology Review*.

Cardoso-Fernandes, J., Lima, A., Roda-Robles, E., and Teodoro, A. C. (2019b). Constraints and potentials of remote sensing data/techniques applied to lithium (Li)-pegmatites. *Can. Mineral.* 57 (5), 72–725. doi:10.3749/canmin.ab00004

Cardoso-Fernandes, J., Lima, A., and Teodoro, A. C. "Potential of sentinel-2 data in the detection of lithium (Li)-bearing pegmatites: a study case," in Proceedings of the SPIE 10790, Earth Resources and Environmental Remote Sensing/GIS Applications IX. Bellingham, WA, October 15, 2018.

Cardoso-Fernandes, J., Teodoro, A. C., Lima, A., Perrotta, M., and Roda-Robles, E. (2020a). Detecting Lithium (Li) mineralizations from space: current research and future perspectives (Review). *Appl. Sci.* 10 (5), 1785. doi:10.3390/app10051785

Cardoso-Fernandes, J., Teodoro, A. C., and Lima, A. (2019a). Remote sensing data in lithium (Li) exploration: a new approach for the detection of Li-bearing pegmatites. *Int J. Appl. Earth Obs. Geoinformation.* 76, 10–25. doi:10.1016/j.jag.2018.11.001

Cardoso-Fernandes, J., Teodoro, A. C., Lima, A., and Roda-Robles, E. (2020b). Semi-automatization of support vector machines to map lithium (Li) bearing pegmatites. *Rem. Sens.* 12, 2319. doi:10.3390/rs12142319

Cerny, P. (1989). "Characteristics of pegmatite deposits of tantalum". in Lanthanides, Tantalum and Niobium. (Berlin, Germany: Springer-Verlag), 195–239.

Cerný, P., and Ercit, T. S. (2005). The classification of granitic pegmatites revisited. *Can. Mineral.* 43 (6), 2005–2026. doi:10.2113/gscanmin.43.6.2005

Chen, D. H., Sui, Q. L., Zhao, X. J., Li, X. T., Gao, Y. B., and Wang, Z. H. (2019). Geochemical characteristics of magnetite from Zankan iron deposit in Tashen-Kuergan orefield and its constraint on mineralization. *Miner. Deposits.* 38 (2), 426–438 [in Chinese with English abstract].

Chen, J. P., Wang, Q., Dong, Q. J., and Cong, Y. (2009). Extraction of remote sensing alteration information in Tuotuohe, Qinghai Province. *Earth Sci. J. China Univ. Geosci.* 34 (2), 314–318 [in Chinese with English abstract].

Chen, Y. T., Zhang, G. W., Lu, R. K., and Zhang, Y. Q. (2010). $^{40}$Ar/$^{39}$Ar geochronology of the Guozhacuo fault in the northwestern margin of Qinghai-Tibet Plateau—new evidence for the western extension of Altyn Tagh fault. *Geol. Bull. China.* 29 (8), 1129–1137 [in Chinese with English abstract].

Cui, Y. R., Tu, J. R., Chen, F., Hao, S., Ye, L. J., Zhou, H. Y., et al. (2017). The research advances in LA-(MC)-ICP-MS U-Pb dating of cassiterite. *Acta Geol. Sin.* 91 (6), 1386–1399 [in Chinese with English abstract].

Dai, J. J., Wang, D. H., Dai, H. Z., Liu, L. J., and Ling, T. Y. (2018). Reflectance spectral characteristics of rocks and minerals in Jiajika lithium deposits in west sichuan. *Miner. Anal.* 37 (5), 507–517 [in Chinese with English abstract].

Dai, J. J., Wang, D. H., Dai, H. Z., Liu, L. J., and Wu, Y. N. (2017). Geological mapping and ore-prospecting study using remote sensing technology in Jiajika area of Western Sichuan Province. *Chin. Geol.* 44 (2), 389–398 [in Chinese with English abstract].

Dimmell, P. M., and Morgan, J. A. (2005). The aubry pegmatites: exploration for highly evolved lithium-cesium-tantalum pegmatites in northern Ontario. *Explor. Min. Geol.* 14, 45–59. doi:10.2113/gsemg.14.1-4.45

Fan, J. J., Tang, G. J., Wei, G. J., Wang, H., Xu, Y. G., Wang, Q., et al. (2020). Lithium isotope fractionation during fluid exsolution: implications for Li mineralization of the Bailongshan pegmatites in the West Kunlun, NW Tibet. *Lithos* 105236 (6), 352–353. doi:10.1016/j.lithos.2019.105236

Fu, X. F., Yuan, L. P., Wang, D. H., Hou, L. W., Pan, M., Hao, X. F., et al. (2015). Mineralization characteristics and prospecting model of newly discovered X03 rare metal vein in Jiajika orefield, Sichuan. *Miner. Deposits.* 34 (6), 1172–1186 [in Chinese with English abstract].

Gan, F. P., Wang, R. S., and Ma, A. N. (2003). Spectral identification tree (sit) for mineral extraction based on spectral characteristics of minerals. *Earth Sci. Front.* 10 (2), 445–454 [in Chinese with English abstract].

Gao, Y. B., Li, K., Teng, J. X., Zhao, X. M., Zhao, X. J., Yan, Z. Q., et al. (2019). Mineralogy, geochemistry and genesis of giant huoshaoyun Zn-Pb deposit in Karakoram area, Xinjiang, NW China. *Northwestern Geol.* 52 (4), 152–169 [in Chinese with English abstract].

Gao, Y. B., Teng, J. X., Chen, D. H., and Sui, Q. L. (2017). Metallogenic geological characteristics and prospecting direction of maerkansu manganese ore belt in west Kunlun, Xinjiang. *Northwestern Geol.* 50 (1), 261–269 [in Chinese with English abstract].

Gao, Y. B., Teng, J. X., Li, W. Y., Chen, D. H., Sui, Q. L., Jing, D. L., et al. (2018). Geology, geochemistry and ore genesis of the aoertuokanashi manganese deposit, West Kunlun, Xinjiang, northwest China. *Acta Petrol. Sinica.* 34 (8), 2341–2358 [in Chinese with English abstract].

Gao, Y. B., Zhao, X. M., Zhao, X. J., Li, K., Teng, J. X., Yan, Z. Q., et al. (2020). Mineralogy, geochemistry and genesis of duobaoshan Zn-Pb deposit in Karakoram, Xinjiang. *Northwestern Geol.* 53 (1), 122–137 [in Chinese with English abstract].

Goodenough, K. M., Shaw, R. A., Smith, M., Estrade, G., Marqu, E., Bernard, C., et al. (2019). Economic mineralization in pegmatites: comparing and contrasting NYF and LCT examples. *Can. Mineral.* 57 (5), 753–755. doi:10.3749/canmin.ab00013

Hao, S., Li, H. M., Li, G. Z., Geng, J. Z., Zhou, H. Y., Xiao, Z. B., et al. (2016). The comparison of the principle and applicability between two methods of deducting the initial common lead for *in situ* LA-ICP-MS U-Pb isotope dating of cassiterite. *Geol. Bull. China.* 35 (4), 622–632 [in Chinese with English abstract].

Hao, X. F., Fu, X. F., Liang, B., Yuan, L. P., Pan, M., and Tang, Y. (2015). Formation ages of granite and X03 pegmatite vein in Jiajika, western Sichuan, and their geological significance. *Miner. Deposits.* 34 (6), 1199–1208 [in Chinese with English abstract].

Harrison, T. M., Célérier, J., Aikman, A. B., Hermann, J., and Heizler, M. T. (2009). Diffusion of 40Ar in muscovite. *Geochem. Cosmochim. Acta.* 73 (4), 1039–1051. doi:10.1016/j.gca.2008.09.038

He, Z. F., Li, D. P., Liu, J., and Zhao, Y. (2009). Late Cenozoic tectono-geomorphic features of the Kangxiwa fault zone, northwestern Tibetan plateau, and its tectonic implication. *Quat. Sci.* 29 (3), 616–624 [in Chinese with English abstract].

Hunt, G. R., and Ashley, R. P. (1979). Spectra of altered rocks in the visible and near infrared. *Econ. Geol.* 74, 1613–1629. doi:10.2113/gsecongeo.74.7.1613

Jia, Q. Z., Li, W. M., and Yu, P. S. (1999). *The Metallogenic condition and prognosis of massive sulfide deposits in west Kunlun: Beijing*. Beijing, China: Geological Publishing House, 1–130 [in Chinese].

Jiang, Y.-H., Jia, R.-Y., Liu, Z., Liao, S.-Y., Zhao, P., and Zhou, Q. (2013). Origin of middle Triassic high-K calc-alkaline granitoids and their potassic microgranular enclaves from the Western Kunlun orogen, northwest China: a record of the closure of Paleo-Tethys. *Lithos.* 156–159, 13–30. doi:10.1016/j.lithos.2012.10.004

Jiang, Y. H., and Yang, W. Z. (2000). Discovery of A-type granite zone and its geodynamic significance in the western Kunlun mountains: China. *Geol. Rev.* 46 (3), 235–244 [in Chinese with English abstract].

Jin, M. S., Wang, H., Qiao, G. B., and Zhang, S. P. (2014). The discovery of heiqia iron mineralization belt in west Kunlun by high resolution remote sensing technology and its. *Geological Significance. Northwestern. Geol.* 47 (4), 221–226 [in Chinese with English abstract].

Jin, M. S., Wang, H., Zhang, W., and Wang, X. (2015). Method for extraction of ferric contamination anomaly from high-resolution remote sensing data and its applications. *Remote Sensing For Land and Resources.* 27 (3), 122–127 [in Chinese with English abstract].

Kendall, M. (1975). *Multivariate analysis.* London, UK: Charles Griffin and Co. Ltd.

Lee, J.-Y., Marti, K., Severinghaus, J. P., Kawamura, K., Yoo, H.-S., Lee, J. B., et al. (2006). A redetermination of the isotopic abundances of atmospheric Ar. *Geochem. Cosmochim. Acta.* 70 (17), 4507–4512. doi:10.1016/j.gca.2006.06.1563

Li, H. K., Geng, J. Z., Hao, S., Zhang, Y. Q., and Li, H. M. (2009). Zircon U-Pb dating technique using LA-MC-ICP-MS. *J. Mineral. Petrol.* S1, 600–601 [in Chinese].

Li, J. K., Liu, X. F., and Wang, D. H. (2014). The metallogenetic regularity of lithium deposit in China. *Acta Geol. Sin.* 88 (12), 2269–2283 [in Chinese with English abstract].

Li, J. K., Wang, D. H., Zhang, D. H., and Fu, X. F. (2007). *Mineralization mechanism and continental geodynamic of pegmatite type deposits in western Sichuan.* Beijing, China: Atomic Energy Press, 1–187 [in Chinese].

Li, K., Gao, Y. B., Teng, J. X., Jin, M. S., and Li, W. (2019). Metallogenic geological characteristics, mineralization age and resource potential of the granite-pegmatite-type rare metal deposits in Dahongliutan area, Hetian County, Xinjiang. *Northwestern. Geol.* 52 (4), 206–221 [in Chinese with English abstract].

Liang, T., Wang, Y., Zhang, Z., Feng, Y., Yang, X., Zhou, Y., et al. (2019). *Study of the zonation of pegmatite veins in the Dahongliutan area, Xinjiang Province.* Xi'an, China: Chang'an University Report, 250 [in Chinese].

Linnen, R. L., Van Lichtervelde, M., and Černý, P. (2012). Granitic pegmatites as sources of strategic metals. *Elements.* 8, 275–280. doi:10.2113/gselements.8.4.275

Liu, L., Feng, J., Benoit, B., Xu, X., Zhou, J., Han, L., et al. (2017a). Mapping alteration using imagery from the Tiangong-1 hyperspectral spaceborne system: example for the Jintanzi gold province, China. *Int. J. Appl. Earth Obs. Geoinf.* 59, 31–41. doi:10.1016/j.jag.2017.02.023

Liu, L. J., Fu, X. F., Wang, D. H., Hao, X. F., Yuan, L. P., and Pan, M. (2015). Geological characteristics and metallogeny of Jiajika-style rare metal deposits. *Miner. Deposits.* 34 (6), 1187–1198 [in Chinese with English abstract].

Liu, L., Wang, D. H., Liu, X. F., Li, J. K., Dai, H. Z., and Yan, W. D. (2017b). The main types, distribution features and present situation of exploration and development for domestic and foreign lithium mine. *Chin. Geol.* 44 (2), 263–278. doi:10.1016/s1876-3804(17)30024-1 [in Chinese with English abstract].

Liu, Q., Yang, K. G., Zhang, C. L., Dong, Y. G., and Guo, K. Y. (2003). The microstructure feature and its geological significance of Kangxiwa Fracture zone, West Kunlun. *J. Mineral. Petrol.* 23 (3), 26–30 [in Chinese with English abstract].

Liu, Y., Gao, S., Hu, Z., Gao, C., Zong, K., and Wang, D. (2010). Continental and oceanic crust recycling-induced melt-peridotite interactions in the Trans-North China Orogen: U-Pb Dating, Hf Isotopes and trace elements in zircons from mantle xenoliths. *J. Petrol.* 51 (1-2), 537–571. doi:10.1093/petrology/egp082

London, D. (2008). *Pegmatites.* The Canadian Mineralogist, Mineralogical Association of Canada, Special Publication 10, 347.

London, D. (2018). Ore-forming processes within granitic pegmatites. *Ore Geol. Rev.* 101, 349–383. doi:10.1016/j.oregeorev.2018.04.020

Ludwig, K. R. (2003). *User's manual for Isoplot 3.00 A geochronological toolkit for Microsoft excel*, 4. Berkeley, CA: Berkeley Geochronology Center, 70.

Mattern, F., and Schneider, W. (2000). Suturing of the proto- and paleo-tethys oceans in the western Kunlun (Xinjiang, China). *J. Asian Earth Sci.* 18, 637–650. doi:10.1016/s1367-9120(00)00011-0

McDougall, I., and Harrison, T. M. (1999). *Geochronology and thermochronology by the 40Ar/39Ar method.* 2nd Edn. New York, NY: Oxford University Press, 269.

Mendes, D., Perrotta, M. M., Costa, M. A. C., and Paes, V. J. C. Mapeamento espectral para identificação de assinaturas espectrais de minerais de lítio em

imagens ASTER (NE/MG). in Proceedings Anais do XVIII simpósio brasileiro de sensoriamento remoto, Santos, Brazil, November 2017, 5273–5280.

Moradi, M., Basiri, S., Kananian, A., and Kabiri, K. (2014). Fuzzy logic modeling for hydrothermal gold mineralization mapping using geochemical, geological, ASTER imageries and other geo-data, a case study in Central Alborz, Iran. *Earth Sci. India.* 8 (1), 197–205. doi:10.1007/s12145-014-0151-9

Mulja, T., and Williams-Jones, A. E. (2018). The physical and chemical evolution of fluids in rare-element granitic pegmatites associated with the Lacorne pluton, Québec, Canada. *Chem. Geol.* 493, 281–297. doi:10.1016/j.chemgeo.2018.06.004

Munk, L. A., Boutt, D. F., Hynek, S. A., and Moran, B. J. (2018). Hydrogeochemical fluxes and processes contributing to the formation of lithium-enriched brines in a hyper-arid continental basin. *Chem. Geol.* 493, 37–57. doi:10.1016/j.chemgeo.2018.05.013

Peng, H. L., He, N. Q., Wang, M. C., Du, B., Li, W. J., and Liu, Y. Q. (2018). Geological characteristics and metallogenic regularity of West Trace 509 rear polymetallic deposit in Dahongliutan region, Hetian, Xinjiang. *Northwestern Geol.* 51 (3), 146–154 [in Chinese with English abstract].

Phillips, D., Matchan, E. L., Honda, M., and Kuiper, K. F. (2017). Astronomical calibration of 40Ar/39Ar reference minerals using high-precision, multi-collector (ARGUSVI) mass spectrometry. *Geochem. Cosmochim. Acta.* 196, 351–369. doi:10.1016/j.gca.2016.09.027

Pour, A. B., and Hashim, M. (2015). Hydrothermal alteration mapping from Landsat-8 data, Sar Cheshmeh copper mining district, south-eastern Islamic Republic of Iran. *J. Taibah Univ. Sci.* 9 (2), 155–166. doi:10.1016/j.jtusci.2014.11.008

Qiao, G. B., Zhang, H. D., Wu, Y. Z., Jin, M. S., Du, W., Zhao, X. J., et al. (2015). Petrogenesis of the Dahongliutan monzogranite in western Kunlun: constraints from SHRIMP zircon U-Pb geochronology and geochemical characteristics. *Acta Geol. Sin.* 89 (7), 1180–1194 [in Chinese with English abstract].

Scogings, A., Porter, R., and Jeffress, G. (2016). Reporting exploration results and mineral resources for lithium mineralised pegmatites. *AIG News Issue.* 125, 32–36.

Selway, J. B., Breaks, F. W., and Tindle, A. G. (2005). A review of rare-element (Li-Cs-Ta) pegmatite exploration techniques for the superior province, Canada, and large worldwide tantalum deposits. *Explor. Min. Geol.* 14, 1–30. doi:10.2113/gsemg.14.1-4.1

Steiger, R. H., and Jäger, E. (1977). Subcommission on geochronology: convention on the use of decay constants in geo- and cosmochronology. *Earth Planet Sci. Lett.* 36, 359–362. doi:10.1016/0012-821x(77)90060-7

Steiner, B. M. (2018). Using stream sediment geochemistry to fingerprint regional geology and mineralisation systems in southeast Ireland. *Ir. J. Earth Sci.* 36, 45–61. doi:10.3318/ijes.2018.36.4

Steiner, B. M. (2019a). W and Li–Cs–Ta signatures in I–type granites—a case study from the Vosges Mountains, NE France. *J. Geochem. Explor.* 197, 238–250. doi:10.1016/j.gexplo.2018.12.009

Steiner, B. M. (2019b). Tools and workflows for grassroots Li-Cs-Ta (LCT) pegmatite exploration. *Minerals.* 9, 499. doi:10.3390/min9080499

Teng, J. X., and Gao, Y. B. (2019). *Investigation and exploration demonstration second-level project of the Fe, Pb and Zn Resource Base in the Western Kunlun area*, Xi'an,China: Xi'an Center of China Geological Survey Report, 526 [in Chinese].

Thomas, R., and Davidson, P. (2016). Revisiting complete miscibility between silicate melts and hydrous fluids, and the extreme enrichment of some elements in the supercritical state - consequences for the formation of pegmatites and ore deposits. *Ore Geol. Rev.* 72, 1088–1101. doi:10.1016/j.oregeorev.2015.10.004

Wang, D. H., Sun, Y., Liu, X. F., Tian, S. H., Dai, J. J., Liu, L. J., et al. (2018). Deep exploration technology and prospecting direction for lithium energy metal. *Geol. Surv. China.* 5 (1), 1–9 [in Chinese with English abstract].

Wang, D., Sun, Y., Dai, H., Guo, W., Zhao, Z., Zhao, T., et al. (2019). Characteristics and exploitation of rare earth, rare metal and rare-scattered element minerals in China. *Chin. J. Chem. Eng.* 21 (1), 119–127. doi:10.15302/j-sscae-2019.01.017 [in Chinese with English abstract].

Wang, H., Gao, H., Zhang, X.-Y., Yan, Q.-H., Xu, Y., Zhou, K., et al. (2020). Geology and geochronology of the super-large Bailongshan Li-Rb-(Be) rare-metal pegmatite deposit, West Kunlun orogenic belt, NW China. *Lithos.* 360-361, 105449. doi:10.1016/j.lithos.2020.105449

Wang, H., Li, P., Ma, H. D., Zhu, B. Y., Qiu, L., and Zhang, X. Y. (2017). Discovery of the Bailongshan superlarge lithium-rubidium deposit in Karakorum, Hetian, Xinjiang, and its prospecting implication. *Geotect. Metallogenia.* 41, 1053–1062 [in Chinese with English abstract].

Wei, X. P., Wang, H., Hu, J., Mu, S. L., Qiu, Z. W., Yan, Q. H., et al. (2017). Geochemistry and geochronology of the Dahongliutan two-mica granite pluton in Western Kunlun orogen: geotectonic implications. *Geochimica.* 46 (1), 66–80 [in Chinese with English abstract].

Xiao, P. X., and Gao, X. F. (2015). *Regional geological survey reports of critical areas in Western Kunlun and Altyn.* Xi'an, China: Xi'an Center of China Geological Survey Reports, 51–68 [in Chinese].

Xiao, W., Han, F., Windley, B. F., Yuan, C., Zhou, H., and Li, J. (2003). Multiple accretionary orogenesis and episodic growth of continents: insights from the western Kunlun Range, Central Asia. *Int. Geol. Rev.* 45, 303–328. doi:10.2747/0020-6814.45.4.303

Xu, Z. Q., Qi, X. X., Yang, J.S., Ji, S. C., Li, H. B., and Chen, F. Y. (2007). Senses and timings of two kinds of shear in the Kangxiwar strike-slip shear zone, West Kunlun, and their tectonic significance. *Geol. Bull. China.* 26 (10), 1252–1261 [in Chinese with English abstract].

Xu, Z. Q., Wang, R. C., Zhao, Z. B., and Fu, X. F. (2018). On the structural backgrounds of the large-scale "hard-rock type" lithium ore belts in China. *Acta Geol. Sin.* 92 (6), 1091–1106 [in Chinese with English abstract].

Yan, Q.-H., Qiu, Z.-W., , H., Wang, M., Wei, X.-P., Li, P., et al. (2018). Age of the Dahongliutan rare metal pegmatite deposit, West Kunlun, Xinjiang (NW China): constraints from LA-ICP-MS U-Pb dating of columbite-(Fe) and cassiterite. *Ore Geol. Rev.* 100, 561–573. doi:10.1016/j.oregeorev.2016.11.010

Yang, J. J., Fang, H. B., Zhang, Y. J., and Chen, W. (2003). Remote sensing anomaly extraction in important metallogenic belts of western China. *Remote Sensing For Land and Resources.* 57 (3), 50–53 [in Chinese with English abstract].

Yang, W. Q. (2013). The Indosinian metamorphism, magmatism and formation age of Bunlunkuole rock group. *Taxkorgan-kangxiwar tectonic belt, western Kunlun.* PhD thesis. Kirkland (WA): Northwest University, 155 [in Chinese with English abstract].

Yao, F. J., Yang, J. M., Zhang, Y. J., and Geng, X. X. (2009). Extraction of remote sensing alteration anomalies of three types of ore deposits and its application. *Acta Petrol. Sinica.* 25 (4), 971–976 [in Chinese with English abstract].

Zhang, C. L., Yu, H. F., Wang, A. G., and Guo, K. Y. (2005). Dating of triassic granites in the western Kunlun mountains and its tectonic significance. *Acta Geol. Sin.* 79 (5), 645–652 [in Chinese with English abstract].

Zhang, Q., Liu, Y., Wu, Z., Huang, H., Li, K., and Zhou, Q. (2018). Late Triassic granites from the northwestern margin of the Tibetan Plateau, the Dahongliutan example: petrogenesis and tectonic implications for the evolution of the Kangxiwa Palaeo-Tethys. *Int. Geol. Rev.* 61 (2), 175–194. doi:10.1080/00206814.2017.1419444

Zhang, W., Zhang, W., Liu, S. Y., Yang, J. Z., and Mao, S. Y. (2011). Automatic interpretation of high resolution remotely sensed images by using kernel method. *Remote Sensing For Land and Resources.* 90 (3), 82–87 [in Chinese with English abstract].

Zhang, Y. J., and Yao, F. J. (2009). Application study of multi-spectral ASTER data for determination of ETM remote sensing anomaly property: taking Wulonggou region of eastern Kunlun mountain range as example. *Acta. Petrol. Sinica.* 25 (4), 963–970 [in Chinese with English abstract].

Zhang, Z., Liang, T., Feng, Y. G., Yang, X. Q., Li, K., Ding, K., et al. (2019). Geologic feature and chronology study of Kangxiwa beryl-bearing muscovite pegmatite in West Kunlun orogenic belt, Xinjiang. *Northwestern Geol.* 52 (1), 75–88 [in Chinese with English abstract].

Zhao, Y. S. (2003). *Principles and methods of remote sensing application analysis.* Beijing, China: Science Press, 155–259 [in Chinese].

Zhou, B., Sun, Y. X., and Kong, D. Y. (2011). Geological features and prospecting potential of rare metallic deposits in the Dahongliutan region, Xinjiang. *Acta Geol. Sichuan.* 31 (3), 288–292 [in Chinese with English abstract].